J Intell Robot Syst (2017) 88:219–246
DOI 10.1007/s10846-017-0545-2

Mathematical Modelling and Control of an Unmanned Aerial Vehicle with Moving Mass Control Concept

Tomislav Haus · Matko Orsag · Stjepan Bogdan

Received: 15 September 2016 / Accepted: 17 March 2017 / Published online: 31 March 2017

Abstract In this paper we present a novel concept of attitude control for a multi-rotor unmanned aerial vehicle by actively controlling its center of gravity. This research is a part of our efforts to build a heavy lift multi-rotor platform capable of carrying over 50 kg of payload. To that end, we propose using miniature two-stroke combustion engines to supply the necessary lift and combine them with moving masses used to control the vehicle attitude. In this paper we present a complete nonlinear dynamical model of such a vehicle and use it to derive the transfer functions of roll and pitch dynamics. Furthermore, we formulate a detailed root-locus based stability and sensitivity analysis of the proposed control scheme and discuss its underlining effect on the mechanical parameter design. We present the experimental testbed, consisted of the vehicle mounted on a 2 degrees of freedom gimbal, and derive necessary conditions for testbed parameters in order to match the testbed and free-flight quadrotor dynamics. Finally, we present simulation results from a Gazebo based simulator and experimental results of the testbed. Both results confirm the findings of our mathematical analysis.

Keywords UAV · Internal combustion engine · Moving mass · Root locus

1 Introduction

The work presented in this paper fits within the scope of an ongoing project called MORUS that aims to build a cooperative autonomous robotic system able to work both in air and underwater (Fig 1). To that end, an unmanned aerial vehicle (UAV) and an autonomous underwater vehicle (AUV) are brought to work together on a common goal, maritime surveillance. In the envisioned scenario, the UAV has to be capable of lifting the AUV and carrying it to a designated drop-off point.

Ever since they were introduced to the mainstream [1], quadrotors have emerged as a number one research platform used in aerial robotics. Since then, numerous linear and nonlinear control algorithms have been proposed and tested. However, these algorithms rely on an underlining control concept where one varies the rotational speed of the propellers. In this paper we aim to explore additional control concepts, namely, how to utilize the shifting center of gravity (CoG) as a driving force for the control of the quadrotor UAV.

T. Haus (✉) · M. Orsag · S. Bogdan
Laboratory for Robotics and Intelligent Control Systems,
Faculty of Electrical Engineering and Computing,
University of Zagreb, Unska 3, 10000 Zagreb, Croatia
e-mail: tomislav.haus@fer.hr

M. Orsag
e-mail: matko.orsag@fer.hr

S. Bogdan
e-mail: stjepan.bogdan@fer.hr

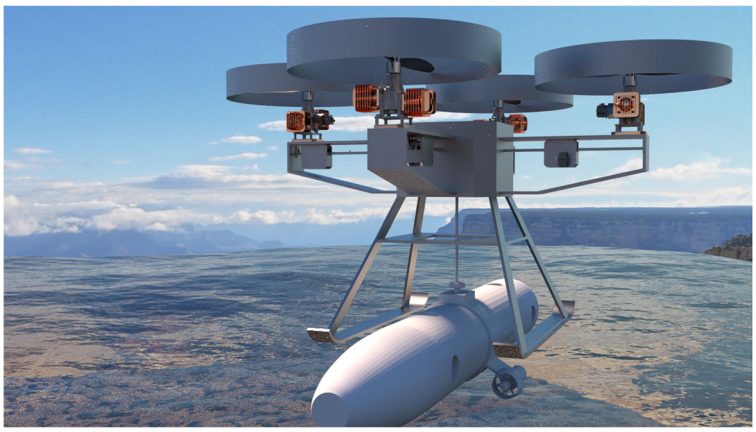

Fig. 1 The goal of the MORUS project is to design a cooperative autonomous robotic system comprised of a UAV and an AUV, working together in a maritime environment

The main incentive behind the proposed control concept is the fact that the proposed mission scenario which we aim to execute requires high power engines capable of sustaining the vehicle and its heavy payload (i.e. > 50 kg) in the air for a long period of time. Even though electrical DC motors have been the backbone of every vertical takeoff and land (VTOL) UAV, this is mostly due to their surpassing dynamical capabilities when compared to internal combustion engines (ICE). However, DC motors fall short in a power-to-weight ratio comparison, which is crucial for lifting heavy objects and sustaining them airborne for a long period of time [2, 3]. Since there are no actual comparisons of ICE and DC motors in micro UAVs, we turn to the findings in [3], where authors compared various engines' performance (i.e. fuel cell, ICE, DC, etc.) in cars, to find that the current state of the art batteries lack the necessary power density in order to archive as long range as gasoline powered IC engines.

Although there has been tremendous advances in the production of small combustion engines, there is a growing concern within the robotics community, that these engines do not have the necessary dynamical capabilities to stabilize the quadrotor in flight. For instance, the authors in [4], proposed a novel concept of a quadrotor powered by a single four stroke ICE, controlled through additional four mechanical variators which distribute power via shafts and gears. The solution proposed in this paper, however, uses four IC engines and controls the UAV by varying the overall CoG with moving masses. This control concept is not new to robotics, and it has been widely studied for the control of underwater vehicles, missiles and space robots [5–8]. However, to the best of authors' knowledge, this type of control has not been implemented or tested on multirotor VTOL platforms. On the other hand, UAV researchers explored the effect of CoG variations [9–12], but only as a disturbance on the control not as a means to control it.

We continue the paper with a complete 6 degrees of freedom (DOF) mathematical model of the free-flight quadrotor. This section helps to introduce the reader to the Sections 3 and 4, where we first we give the comparison of the moving mass control and classical rotor speed control. Next, the dynamical performance and sensitivity analysis is given in order to determine values of some important mechanical parameters. We conclude the paper with simulation results in a Gazebo environment (Section 5) and experimental results of a laboratory testbed (Section 6).

2 Mathematical Model of the Quadrotor with Moving Mass Control

In this section we first derive a 6DOF nonlinear model describing the vehicle's translation and rotation. From there, we linearize the attitude model to get a transfer function suitable for control design, given in Section 2.2. We also derive the linearized model of the experimental testbed and compare it with the attitude model of the free-flight UAV (Section 2.3).

All vectors used in this section are expressed in the moving reference frame, i.e. the quadrotor body frame denoted as L_0 in Fig. 2. An exception is the gravity force vector which we conveniently express in the inertial frame L_I. Next, coordinate frame L_{CoG} is the frame aligned with L_0 and attached to the

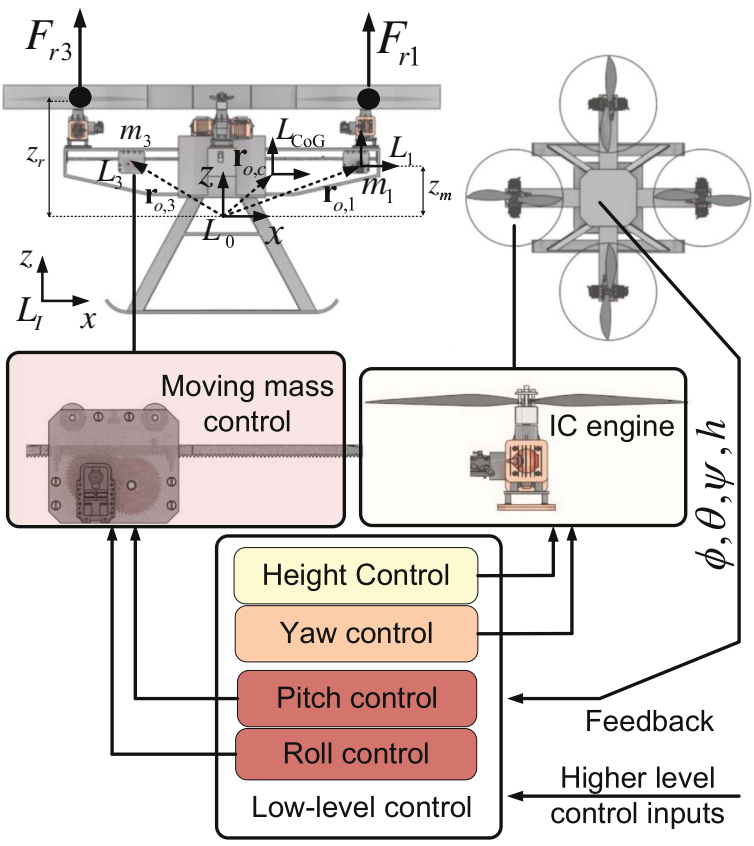

Fig. 2 MMC controls the pitch and roll angle attitude. Together with classic rotor speed commands, which control yaw angle and height of the vehicle, it forms a classic low level attitude controller of the multirotor UAV. The figure shows quadrotor coordinate frames: Main body L_0, moving masses L_1, L_3 and the center of gravity L_{CoG}. Showing only pitch attitude dynamics for clarity. The connection between the frames i and j is denoted with vector $\mathbf{r}_{i,j}$

vehicle CoG. Note that we express angular momentum and angular velocities w.r.t. the vehicle's CoG (L_{CoG} frame). We use the following notation for radius and velocity vectors: $\boldsymbol{r}_c$ denotes radius vector from the inertial frame to the L_{CoG} frame while $\boldsymbol{r}_{0,c}$ denotes radius vector from the L_0 frame to the L_{CoG}. Velocity $\boldsymbol{v}_c$ denotes the velocity of the L_{CoG} frame w.r.t the inertial frame while $\boldsymbol{v}_{0,c}$ denotes the velocity of the L_{CoG} frame w.r.t the L_0 frame.

2.1 Nonlinear Dynamical Model of the UAV with MMC

Moving Mass Control (MMC) is a concept that relies on the change of CoG of the vehicle to ultimately distribute torque around the body in order to control its attitude. In total, a multirotor has 6 DOF, and in our implementation MMC controls only two of them, roll and pitch angle. Since the underlining physics of MMC cannot effectively control its other degrees of freedom, classical rotor speed control is applied to yaw angle and height control. The only two DOFs left (i.e. x-axis and y-axis) are controlled through high level controllers, and thus fall out of scope of this paper. The control structure is presented in Fig 1.

Mathematical modelling starts with the well known formula for the time derivative of an arbitrary vector $\boldsymbol{r}_0$ expressed in the moving reference frame L_0 (body frame), w.r.t. the inertial frame [13]:

$$\frac{d^{\omega}}{dt}(\boldsymbol{r}_0) = \dot{\boldsymbol{r}}_0 + \boldsymbol{\omega} \times \boldsymbol{r}_0, \tag{1}$$

where $\dot{\boldsymbol{r}}_0$ is vector rate of change in the moving reference frame. On the right side of the equation, ω represents angular velocity of the moving reference frame w.r.t. the inertial frame. In this paper ω represents the quadrotor's angular velocity. Note that $\frac{d^{\omega}}{dt}$ denotes the time derivative of a vector expressed in the moving frame w.r.t the inertial frame.

The CoG of the vehicle observed in the body frame is given by:

$$\boldsymbol{r}_{0,c} = \frac{m_b \boldsymbol{r}_{0,b} + \sum_{i=1}^{4} m_i \boldsymbol{r}_{0,i}}{m_b + \sum_{i=1}^{4} m_i} = \frac{\sum_{i=1}^{4} m_i \boldsymbol{r}_{0,i}}{M}, \tag{2}$$

where m_b as the mass of the quadrotor rigid body (without moving masses), m_i denotes the mass value of a moving mass, M as the total mass of the vehicle, $\boldsymbol{r}_{0,i}$ and $\boldsymbol{r}_{0,b}$ represent the positions of the i-th mass and quadrotor body, respectively, expressed in the body frame. Note that we used the assumption that the origin of the body frame coincides with the CoG of the quadrotor rigid body (i.e. the frame without moving masses), which yields $\boldsymbol{r}_{0,b} = 0$.

Using (2), we can express the velocity of the CoG frame ($\boldsymbol{v}_c$) w.r.t the inertial frame

$$\boldsymbol{v}_c = \boldsymbol{v}_0 + \boldsymbol{v}_{0,c} + \boldsymbol{\omega} \times \boldsymbol{r}_{0,c}, \tag{3}$$

with $\boldsymbol{v}_0$ as the velocity of L_0 w.r.t the inertial frame and $\boldsymbol{v}_{0,c}$ as the velocity of L_{CoG} frame w.r.t the L_0 frame. Note that $\boldsymbol{v}_{0,c}$ is simply computed as time derivative of (2)

$$\boldsymbol{v}_{0,c} = \frac{\sum_{i=1}^{4} m_i \dot{\boldsymbol{r}}_{0,i}}{M}. \tag{4}$$

Similarly, the velocity of the i-th moving mass ($\boldsymbol{v}_i$) w.r.t. the inertial frame can be expressed as

$$\boldsymbol{v}_i = \boldsymbol{v}_0 + \boldsymbol{v}_{0,i} + \boldsymbol{\omega} \times \boldsymbol{r}_{0,i}, \tag{5}$$

with $\boldsymbol{v}_{0,i}$ denoting relative velocity of the i-th mass w.r.t. the quadrotor rigid body (L_0 frame). Using (3) and (5) we compute the velocity of the i-th moving mass as the function of $\boldsymbol{v}_c$ velocity

$$\boldsymbol{v}_i = \boldsymbol{v}_c + \boldsymbol{v}_{0,i} - \boldsymbol{v}_{0,c} + \boldsymbol{\omega} \times \boldsymbol{r}_{c,i}, \tag{6}$$

with $\boldsymbol{r}_{c,i}$ denoting the position of the i-th mass in the L_{CoG} frame. Linear momentum of the i-th mass w.r.t. the inertial frame is given by:

$$\boldsymbol{L}_i = m_i \cdot \boldsymbol{v}_i. \tag{7}$$

By definition, the time derivative of the linear momentum equals the sum of all external forces acting on the i-th mass:

$$\frac{d^{\omega}}{dt}\boldsymbol{L}_i = \sum_{k=1}^{3} \boldsymbol{f}_{ik}, \tag{8}$$

where we distinguish three external forces:

– The force of the motor that controls the mass motion:

$$\boldsymbol{f}_{i1} = K_m T_r U_i \left(\sin(\frac{\pi}{2}i)\hat{\boldsymbol{i}} - \cos(\frac{\pi}{2}i)\hat{\boldsymbol{j}}\right), i \in \{1, 2, 3, 4\}, \tag{9}$$

where K_m is a motor constant, T_r is a transmission ratio, U_i is voltage applied to the motor and $\hat{\boldsymbol{i}}$, $\hat{\boldsymbol{j}}$ as the unit vectors of the L_0 frame in x- and y-direction, respectively.

– The gravity force:

$$\boldsymbol{f}_{i2} = -m_i \cdot g\hat{\boldsymbol{K}}, \tag{10}$$

where $\hat{\boldsymbol{K}}$ is the unit vector in z-direction of the inertial frame, g is the gravity constant.

– Drag force which is simply modelled to be proportional to the moving mass velocity with drag coefficient c_d:

$$\boldsymbol{f}_{i3} = -c_d \cdot \boldsymbol{v}_{0,i}. \tag{11}$$

To compute linear acceleration of the i-th control mass w.r.t. the body frame, we combine (5) and (8) to yield:

$$\frac{d^{\omega}}{dt}\boldsymbol{v}_{0,i} = \frac{1}{m_i}\left(\sum_{k=1}^{3} \boldsymbol{f}_{ik}\right) - \frac{d^{\omega}}{dt}\left(\boldsymbol{v}_0 + \boldsymbol{\omega} \times \boldsymbol{r}_{0,i}\right). \tag{12}$$

Next, we model the linear momentum of the overall system. By definition, we write:

$$\boldsymbol{L}_s = \boldsymbol{L}_b + \sum_{i=1}^{4} \boldsymbol{L}_i, \tag{13}$$

where $\boldsymbol{L}_b$ is the linear momentum of the quadrotor body and $\boldsymbol{L}_i$ is the linear momentum of the i-th moving mass. However, noting that $\boldsymbol{v}_{0,b} = \boldsymbol{0}$ and using (2),(5), one can derive:

$$\begin{aligned} \boldsymbol{L}_s &= M\left(\boldsymbol{v}_0 + \boldsymbol{\omega} \times \boldsymbol{r}_{0,c}\right) + \sum_{i=1}^{4} m_i \boldsymbol{v}_{0,i} \\ &= M\left(\boldsymbol{v}_0 + \boldsymbol{\omega} \times \boldsymbol{r}_{0,c}\right) + \sum_{i=1}^{4} \boldsymbol{L}_{0,i}, \end{aligned} \tag{14}$$

with $\boldsymbol{v}_0$ as the velocity of the quadrotor rigid body w.r.t. the inertial frame and $\boldsymbol{L}_{0,i} = m_i \boldsymbol{v}_{0,i}$ represents the linear momentum of the i-th mass w.r.t the quadrotor rigid body.

Finally, using the definition of linear momentum rate of change, we get the expression for the vehicle's rigid body acceleration:

$$\frac{d^{\omega}}{dt}\boldsymbol{v}_0 = \frac{1}{M}\left(\sum_{j=1}^{4} \boldsymbol{F}_{r_j} + \boldsymbol{F}_g - \frac{d^{\omega}}{dt}\sum_{i=1}^{4} \boldsymbol{L}_{0,i}\right) - \frac{d^{\omega}}{dt}(\boldsymbol{\omega} \times \boldsymbol{r}_{0,c}). \tag{15}$$

External forces applied to the system include rotors' thrust and gravity (drag is neglected). The thrust produced by each rotor is given by simplified, but widely used, quadratic expression:

$$\boldsymbol{F}_{r_j} = b_f \Omega_j^2 \hat{\boldsymbol{k}}, \tag{16}$$

where Ω_j is the j-th rotor speed, b_f is motor constant, $\hat{\boldsymbol{k}}$ is the unit vector in z-direction of the body frame. We assume that the rotor speed is controlled and its closed loop can be described as:

$$T_r \dot{\Omega}_j + \Omega_j = \Omega_{r,j}, \tag{17}$$

with T_r as time constant of a rotor powered with a gas motor and $\Omega_{r,j}$ as a rotor speed reference.

The gravity force expressed in the inertial frame is given by:

$$\boldsymbol{F}_g = -Mg\hat{\boldsymbol{K}}. \tag{18}$$

To model angular motion, we use the definition of the angular momentum w.r.t inertial frame expressed in the L_{CoG} frame combined with (6):

$$\boldsymbol{H}_s = \boldsymbol{H}_b + \sum_{i=1}^{4} \boldsymbol{H}_i \tag{19}$$

$$\begin{aligned}\boldsymbol{H}_b &= \int_k \boldsymbol{r}_{c,k} \times (\boldsymbol{v}_k dm_k) \\ &= \int_k \boldsymbol{r}_{c,k} \times (\boldsymbol{v}_c + \boldsymbol{v}_{0,k} - \boldsymbol{v}_{0,c} + \boldsymbol{\omega} \times \boldsymbol{r}_{c,k}) dm_k \end{aligned} \tag{20}$$

$$\begin{aligned}\boldsymbol{H}_i &= \int_{j_i} \boldsymbol{r}_{c,j_i} \times (\boldsymbol{v}_{j_i} dm_{j_i}) \\ &= \int_{j_i} \boldsymbol{r}_{c,j_i} \times (\boldsymbol{v}_c + \boldsymbol{v}_{0,i} - \boldsymbol{v}_{0,c} + \boldsymbol{\omega} \times \boldsymbol{r}_{c,j_i}) dm_{j_i}, \end{aligned} \tag{21}$$

where $\boldsymbol{H}_s$ is the angular momentum of the overall system, $\boldsymbol{H}_b$ is the angular momentum of the quadrotor rigid body and $\boldsymbol{H}_i$ is the angular momentum of the i-th mass. By dm_k we denote the k-th infinitesimal part of the quadrotor rigid body, $\boldsymbol{v}_k$ represents its velocity and $\boldsymbol{r}_{c,k}$ is the vector from the CoG to the k-th part. Note that by the definition of the rigid body, the velocity of the k-th part w.r.t the body frame equals zero ($\boldsymbol{v}_{0,k} = \boldsymbol{0}$).

Using the definiton of the moment of inertia (MoI) combined with (2), one gets:

$$\boldsymbol{H}_s = \boldsymbol{I}_s^c \boldsymbol{\omega} + \sum_{i=1}^{4} \boldsymbol{r}_{c,i} \times \boldsymbol{L}_{0,i}. \tag{22}$$

where $\boldsymbol{I}_s^c$ is the overall moment of inertia of the system w.r.t. the vehicle CoG. The overall moment of inertia can be computed by summing inertial contributions of each part of the vehicle:

$$\boldsymbol{I}_s^c = \boldsymbol{I}_b^c + \sum_{i=1}^{4} \boldsymbol{I}_i^c, \tag{23}$$

where $\boldsymbol{I}_b^c$ is the moment of inertia of the quadrotor rigid body (3×3 matrix) and $\boldsymbol{I}_i^c$ is the moment of inertia of the i-th moving mass (3×3 matrix). To compute these moments of inertia we use Steiner's theorem, formally known as Parallel axis theorem:

$$\boldsymbol{I}_i^c = \boldsymbol{I}_i + m_i \left(\boldsymbol{r}_{c,i}^\top \cdot \boldsymbol{r}_{c,i} \boldsymbol{E}_3 - \boldsymbol{r}_{c,i} \cdot \boldsymbol{r}_{c,i}^\top \right), \tag{24}$$

where $\boldsymbol{I}_i$ is the moment of inertia of the i-th part w.r.t. its own CoG, and $\boldsymbol{E}_3$ is a 3×3 identity matrix.

The expression for angular velocity rate can be derived from the following equation:

$$\frac{d^\omega}{dt} \left(\boldsymbol{I}_s^c \boldsymbol{\omega} + \sum_{i=1}^{4} \boldsymbol{r}_{c,i} \times \boldsymbol{L}_{0,i} \right) = \sum_{j=1}^{4} \left(\boldsymbol{M}_{f_j} + \boldsymbol{M}_{d_j} \right) + \boldsymbol{M}_g. \tag{25}$$

We model three types of external moments acting on the vehicle:

– The moments of the rotor forces acting on some radius from CoG:

$$\boldsymbol{M}_{f_j} = \boldsymbol{r}_{c,r_j} \times \boldsymbol{F}_{r_j} = (\boldsymbol{r}_{c,o} + \boldsymbol{r}_{o,r_j}) \times \boldsymbol{F}_{r_j}, \tag{26}$$

where $\boldsymbol{r}_{o,r_j}$ is the vector from the body frame origin to the j-th rotor.

– The rotor moments due to the induced drag:

$$\boldsymbol{M}_{d_j} = \zeta_j b_m b_f \Omega_j^2 \hat{\boldsymbol{k}}, \tag{27}$$

where b_m is the moment constant of the propulsion system, $\zeta_j = 1$ if j-th propeller is clockwise (rotors 1 and 3) and $\zeta_j = -1$ if the propeller is counter-clockwise (rotors 2 and 4).

– The moment $\boldsymbol{M}_g$ due to the gravity forces

$$\boldsymbol{M}_g = \boldsymbol{r}_{c,b} \times (-m_b g \hat{\boldsymbol{K}}) + \sum_{i=1}^{4} \boldsymbol{r}_{c,i} \times (-m_i g \hat{\boldsymbol{K}}), \tag{28}$$

where $\boldsymbol{r}_{c,b}$ and $\boldsymbol{r}_{c,i}$ denote position of the quadrotor rigid body and i-th moving mass w.r.t. the CoG. It can be easily shown that $\boldsymbol{M}_g = \boldsymbol{0}$ as we are expressing angular momentum w.r.t. the system CoG.

We use standard Euler angles representation for the vehicle attitude. To get from the inertial frame to the body frame, we assume that the vehicle is first rotated around z-axis for yaw angle ψ, followed by the rotation around body y-axis for pitch angle θ and finally rotation around body x-axis for roll angle ϕ. In the following section we consider small angular velocities for which the roll and pitch rates can be approximated by ω_x and ω_y, respectively.

2.2 Linearized Dynamical Model of the UAV

Attitude controllability through the shift of the vehicle CoG is the main focus of this paper. To that end we derive a transfer function that describes the rate of change of the vehicle's angular velocity w.r.t. the change of the moving masses position. We will give this analysis for pitch dynamics, but the same holds for roll dynamics due to the vehicle symmetry. In the derivation of the transfer function, we linearize the equations in near hover condition which assumes small angular velocity. As a consequence, we neglect gyroscopic terms, euler terms and centrifugal terms that arise from the analysis in the moving frame of reference. Furthermore, we consider that the mass servo system ensures PT_2S dynamics of the mass position response to a given reference:

$$\frac{x_i}{x_{i,ref}}(s) = \frac{1}{\frac{s^2}{\omega_{mm}^2} + \frac{2\zeta_{mm}}{\omega_{mm}}s + 1}, \tag{29}$$

where x_i is the position of the i-th mass in the body coordinate frame, ω_{mm} and ζ_{mm} as the servo system natural frequency and damping. Note that in our previous work [14, 15] we modelled the moving mass dynamics as PT_1 term, but from the experiments with our new moving mass mechanism presented in this paper, we observed that the second order model closely describes this dynamics. For the considered pitch dynamics, we control the position of masses 1 and 3 displace the CoG in the body frame x-direction.

The moving masses positions in the body reference frame (see Fig. 2) are given by:

$$\boldsymbol{r}_{0,i} = \left[\, \sin(\tfrac{\pi}{2}i)L/2 + x_i \;\; 0 \;\; z_m \,\right]^T, \; i \in \{1, 3\} \tag{30}$$

$$\boldsymbol{r}_{0,j} = \left[\, 0 \;\; -\cos(\tfrac{\pi}{2}j)\tfrac{L}{2} + y_j \;\; z_m \,\right]^T, \; j \in \{2, 4\}, \tag{31}$$

where $L/2$ is the initial position of the mass (half of the length L of the motor arm), x_1, x_3 are mass 1 and 3 displacements in body x-axis, y_2, y_4 are mass 2 and 4 displacements in body y-axis and z_m is a mass displacement in body z-axis. Note that we model z_m to be a constant displacement from the body origin, which is the result of the vehicle geometry.

Substituting (30)–(31) into (2), with the assumption of an equal weight of the moving masses, we get the expression for CoG w.r.t. the body frame:

$$\boldsymbol{r}_{0,c} = \mu \cdot \left[\, (x_1 + x_3) \;\; (y_2 + y_4) \;\; 4z_m \,\right]^T, \tag{32}$$

where we introduced μ as a ratio of a moving mass weight and total vehicle weight ($\mu = \frac{m}{M}$).

Next, the position of the rotors in the L_0 frame is given by:

$$\boldsymbol{r}_{0,r_j} = \left[\sin(\frac{\pi}{2}j)L \;\; -\cos(\frac{\pi}{2}j)L \;\; z_r\right]^T, \; j \in \{1, 2, 3, 4\}, \tag{33}$$

with z_r as a vertical displacement of the rotors from the L_0. Using (26), (32), (33) and assuming all rotor forces equal $F_{r,j}|_0$, we compute the moments produced by rotor forces:

$$\sum_{j=1}^{4} \boldsymbol{M}_{f_j} = \left[(F_{r,2} - F_{r,4})L \;\; (F_{r,3} - F_{r,1})L \;\; 0\right]^T + \sum_{j=1}^{4} F_{r,j}\left[-\mu(y_2 + y_4) \;\; \mu(x_1 + x_3) \;\; 0\right]^T, \tag{34}$$

with $F_{r,j}$ denoting the magnitude of the j-th rotor force.

Now we expand (25) and extract expressions for angular velocity in y - axis. After neglecting tensor

products that occur in $\mathbf{I}_s^c$ and $\dot{\mathbf{I}}_s^c$ due to the CoG shift and modelling a moving mass inertial properties as a point mass, we get:

$$\begin{aligned} I_{yy}\dot{\omega}_y = &\sum_{j=1}^{4} \boldsymbol{M}_{f_j} \cdot \hat{\boldsymbol{j}} - (I_{xx} - I_{zz})\omega_x\omega_z \\ &-2m_b\mu^2(x_1 + x_3)(\dot{x}_1 + \dot{x}_3)\omega_y \\ &-2m\frac{l}{2}(\dot{x}_1 - \dot{x}_3)\omega_y \\ &-2m(\dot{x}_1x_1 + \dot{x}_3x_3)(1 - 2\mu + 2\mu^2)\omega_y \\ &+4m(\dot{x}_1x_3 + \dot{x}_3x_1)\mu(1-\mu)\omega_y \\ &+m\omega_z(\dot{y}_2 + \dot{y}_4)z_m(1 - 4\mu) \\ &+m\omega_x\mu((y_2 + y_4)(\dot{x}_1 + \dot{x}_3) \\ &-(\dot{y}_2 + \dot{y}_4)(x_1 + x_3)) \\ &-m(\ddot{x}_1 + \ddot{x}_3)z_m(1 - 4\mu), \end{aligned} \tag{35}$$

with I_{xx}, I_{yy}, I_{zz} as nominal moments of inertia in x-, y- and z-axis, respectively. These moments are computed for the initial positions of the moving masses in the center of each motor arm. The second term in the RHS of (35) is a gyroscopic term which is common to a 3D rigid body dynamics. The third, fourth, fifth and sixth terms stem form the moment of inertia change (i.e. from $\dot{\boldsymbol{I}}_s^c\boldsymbol{\omega}$), while the seventh and eight terms are the result of $\omega \times \sum_{i=1}^{4} \boldsymbol{r}_{c,i} \times \boldsymbol{L}_{0,i}$ projected in the body y-axis. Finally, the ninth term is the y-component of $\sum_{i=1}^{4} \boldsymbol{r}_{c,i} \times \dot{\boldsymbol{L}}_{0,i}$. Note that it can be shown that $\sum_{i=1}^{4} \dot{\boldsymbol{r}}_{c,i} \times \boldsymbol{L}_{0,i} = \boldsymbol{0}$, and therefore there is no contribution of that term to the attitude dynamics.

Now we introduce u_θ as a control input for pitch dynamics:

$$u_\theta = x_{1,ref} = x_{3,ref}, \tag{36}$$

where $x_{1,ref} = x_{3,ref}$ are reference values for mass 1 and 3 position, respectively. Then from (29) the following holds:

$$x_1(s) = x_3(s) = \frac{u_\theta}{\frac{s^2}{\omega_{mm}^2} + \frac{2\zeta_{mm}}{\omega_{mm}}s + 1} \tag{37}$$

Next, we claim that dominant pitch dynamics in near hover condition stems from the first and ninth term in (35). Neglecting other terms in (35), using (34) and (37) , we derive the following transfer function:

$$\frac{\omega_y(s)}{u_\theta(s)} = \frac{2mg - 2m(1-4\mu)z_m s^2}{I_{yy}s(\frac{s^2}{\omega_{mm}^2} + \frac{2\zeta_{mm}}{\omega_{mm}}s + 1)}, \tag{38}$$

where we assumed that the thrust of a single rotor in the hovering state is $F_{r,j}|_0 = \frac{Mg}{4}$.

The transfer function (38) is valid for in-hover condition. For non-hover conditions, the assumption $F_{r,j}|_0 = \frac{Mg}{4}$ is not valid any more. From the second term in RHS of (34), we conclude that the system gain would change if $F_{r,j}$ varies. In particular, if the vehicle is ascending ($F_{r,j} > F_{r,j}|_0$), the gain would be increased, and the opposite happens when the vehicle is descending. For the horizontal motion, we expect that the rotor drag forces, which are proportional to horizontal velocity and rotor speed [16, 17], would produce some influence on attitude dynamics, particularly if the rotors are significantly displaced from the CoG ($z_r >> 0$). We will address the model and influence of these forces in our future work.

In this paper we address the controller design in discrete domain. To that end, we give the discrete transfer function of (38) using the parameters from Table 1 and ZOH transformation:

$$\frac{\omega_y(z)}{u_\theta(z)} = \frac{-0.03377z^2 + 0.06832z - 0.03379}{z^3 - 2.724z^2 + 2.473z - 0.749}. \tag{39}$$

2.3 Linearized Dynamical Model of an Experimental Testbed

In order to test the proposed algorithm we developed a 2 DOF laboratory testbed shown in Fig. 3. The full scale UAV that we have recently developed is fixed to a gimbal which is free to rotate around a center point of rotation (roll and pitch angle). Although the ICE engines and rotors are mounted on the vehicle, in this experimental testbed we do not used them to produce forces and torques. Furthermore, since the gimbal is constrained to rotate around a fixed point, there are some substantial differences between the gimbal model and free-flight quadrotor model. Therefore in this section, we derive the model of the testbed from the afore disseminated free-flight quadrotor model.

Table 1 Model parameters

Symbol	Value and unit	Description
I_{xx}	6.8 kgm^2	Quad. overall MoI (roll)
I_{yy}	6.5 kgm^2	Quad. overall MoI (pitch)
m	1 kg	Moving mass weight
M	34 kg	Vehicle overall weight
b_f	4.56e-4 kg ·m	Thrust constant of the gas motor
b_m	0.01	Moment constant of the gas motor
ω_0	427.4311 rad/s	Rotors velocity in hover
L	0.84 m	Motor arm length
ν	0.92	The ratio of MoI without and with masses
ω_{mm}	17 rad/s	Natural frequency of the mass servo system
ζ_{mm}	0.85 rad/s	Damping factor of the mass servo system
T_r	0.2 s	Time constant of the rotor
Δl	±0.25 m	maximum displacement of the mass
z_m	0.05 m	Vertical displacement of the mass plane
T_s	0.01 s	Sampling time of the discrete system

In order to maintain mathematical consistency throughout the paper, we propose representing the fixed point of rotation as having infinite mass and infinitesimally small tensor of inertia. This observation allows us to calculate the center point of rotation of the laboratory testbed using (2):

$$\boldsymbol{r}_{0,c} = \lim_{M\to\infty} \frac{m_b \boldsymbol{r}_{0,b} + \sum_{i=1}^{4} m_i \boldsymbol{r}_{0,i}}{M} = \mathbf{0}. \tag{40}$$

It is also worth noting that using this formulation linear velocity of the system (15) approaches zero (i.e. standstill)

$$\lim_{M\to\infty} \boldsymbol{v}_0 = \mathbf{0}.$$

When one applies the same reasoning to angular motion, the fixed z axis of the testbed is modelled as infinite moment of inertia, while the x and y axes, which are free to rotate, ideally have a finite value. Therefore, one can write:

$$\mathbf{I}_{gb} = \begin{bmatrix} I_{xx} & 0 & 0 \\ 0 & I_{yy} & 0 \\ 0 & 0 & \infty \end{bmatrix}, \tag{41}$$

thus effectively constraining the angular motion only around body x and y axes (roll and pitch angle).

It turns out that the most significant effect on the motion dynamics comes from the component $\boldsymbol{r}_{c,i} \times \dot{\boldsymbol{L}}_{0,i}$. Since the L_{CoG} is static for this experimental testbed, it holds $\boldsymbol{r}_{c,i} = \boldsymbol{r}_{0,i}$. Therefore, the positions of the masses w.r.t. L_{CoG} is given by (30) and (31). Computing $\boldsymbol{r}_{c,i} \times \dot{\boldsymbol{L}}_{0,i}$ term, one gets:

$$\sum_{i=1}^{4} \boldsymbol{r}_{c,i} \times \dot{\boldsymbol{L}}_{0,i} = 2m_i \left[-z_m \dot{y}_i \;\; z_m \dot{x}_i \;\; x_i \dot{y}_i - y_i \dot{x}_i \right]^T. \tag{42}$$

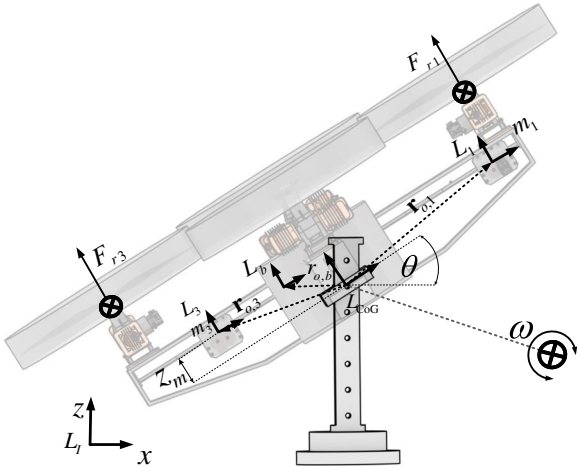

Fig. 3 The figure shows the gimbal testbed coordinate frames. Note that for the gimbal case L_0 and L_{CoG} coincide. Therefore, we introduced the coordinate frame L_b attached to the quadrotor rigid body CoG. For the free-flight quadrotor L_b and L_0 coincide (see Fig. 2)

Just like in the free-flight quadrotor dynamics, z_m plays a crucial role in system dynamics. Since the gimbal is not free to rotate in yaw axis, the z component of (42) has no influence on gimbal dynamics.

The second part of the system dynamics are torques acting on the system. Since we do not use rotors and neglect drag and friction torques, the only torques left acting on the system come from the gravity torque (28), which for the gimbal case does not equal zero. During the experiments we have discovered that the position of the quadrotor rigid body $\boldsymbol{r}_{c,b}$ plays an important role in gimbal dynamics. Therefore, in this paper we analyze in details (28) for $\boldsymbol{r}_{c,b} \neq \boldsymbol{0}$. The position of the quadrotor rigid body (L_b frame) mounted on the gimbal can be expressed as:

$$\boldsymbol{r}_{c,b} = \boldsymbol{r}_{o,b} = \begin{bmatrix} x_b & y_b & z_b \end{bmatrix}^T. \tag{43}$$

Using (30), (31) and (43) we expand (28) in pitch axis which yields:

$$M_{g,y} = \boldsymbol{M}_g \cdot \hat{\boldsymbol{j}} = g\,(m(x_1 + x_3)\cos(\theta) - 2mz_m \sin(\theta) + m_b x_b \cos(\theta) - m_b z_b \sin(\theta)). \tag{44}$$

We linearize (44) by assuming small pitch angle which yields $\cos\theta \approx 1$ and $\sin\theta \approx \theta$. Now if the following conditions are satisfied:

$$z_m\theta \approx 0,\ \ x_b \approx 0,\ \ z_b\theta \approx 0, \tag{45}$$

then we can show that linearized gimbal pitch dynamics is identical to the linearized pitch dynamics of the free-flight quadrotor. Using (45), one can write the dynamics equation of the gimbal:

$$\frac{d^{\omega}}{dt}\left[I_{yy}\omega + mz_m(\dot{x}_1 + \dot{x}_3)\right] = m(x_1 + x_3)g. \tag{46}$$

The aforementioned equation clearly shows that, if (45) holds, one can observe gimbal dynamics as a special case of general quadrotor motion, where $M >> \sum_{i=1}^{4} m_i$ and consequently $\lim_{M\to\infty}\mu = 0$. When we include the mass servo system dynamics and apply the same linearization reasoning as in Section 2.2, we get the linearized transfer function of the laboratory testbed:

$$\frac{\omega_y(s)}{u_\theta(s)} = \frac{2mg - 2mz_m s^2}{I_{yy}s(\frac{s^2}{\omega_{mm}^2} + \frac{2\zeta_{mm}}{\omega_{mm}}s + 1)}. \tag{47}$$

It is easy now to show that (38) reduces to (47) when $\lim_{M\to\infty}\mu = 0$.

Conditions (45) can be easily interpreted as follows: The gimbal axes of rotation should be mounted as close as possible to the vehicle CoG, yielding $x_b \approx y_b \approx z_b \approx 0$. The moving masses vertical displacement should be also kept close to zero ($z_m \approx 0$). Finally, the gimbal should not exhibit large roll and pitch angles, as it then holds $\sin(\theta) \approx \sin(\phi) \approx 0$.

3 The Moving Mass Control vs Traditional Attitude Control

In this section we compare two concepts of attitude control for multi-rotor UAVs, MMC versus classical rotor speed control. It obviously follows from (26) that one can control the torques produced on the vehicle in two ways: In the proposed approach (MMC), rotor torque is controlled by changing the relative distance between a rotor and the controlled CoG (i.e. $\sum \boldsymbol{r}_{c,o} + \boldsymbol{r}_{o,m_j}$); On the other hand rotor speed control achieves this effect by varying the rotor speed which consequently changes thrust $\sum F_{r_j}$. It is important to note that the torque required to control the attitude is in both cases produced by rotor forces.

We can now express the pitching angular rate transfer function w.r.t. small rotor velocity change, typical for a traditional control, as [16]:

$$\frac{\omega_y(s)}{\Delta\Omega(s)} = \frac{4b_f\omega_0 L}{\nu I_{yy}s(T_r s + 1)}, \tag{48}$$

where b_f denotes rotor force constant, ω_0 represents rotor speed in hover, I_{yy} is the MoI of the vehicle in y-axis with masses and ν represents the ratio of the vehicle's moments of inertia without masses and with masses. For the complete list of parameters see Table 1.

Comparing the transfer function of the MMC control concept (38) with the traditional approach (48), one can conclude that there are two major differences: the first is the existence of system zeros in (38) and the second in the actuator dynamics (PT_1 vs PT_2S). One should not neglect the system zeros in controller design as it could deteriorate system performance, or even cause instability as it will be shown in the next section. The position of zeros depends on the vertical mass displacement w.r.t. CoG ($(1-4\mu)z_m$), which means that altering the vertical position of masses changes system dynamics. This is a valuable insight into system dynamics which will be considered in the mechanical design of the vehicle.

When it comes to the actuator dynamics, in our previous work [14, 15] we assumed that the moving mass servo system exhibits PT_1 dynamics, similar to the rotor dynamics (17). In this work, we identify the dynamics of the designed moving mass mechanism as a PT_2S term (see Section 6) and repeat the frequency analysis from [15]. The assumptions used in [15] are valid also here. First, we consider the mass plane and rotors plane to be in the same vertical level as the vehicle CoG. As a consequence, the zeros from (38) cease to exist. Furthermore, we make an assumption that the dynamics of a rotor powered by a gas motor is similar to the dynamics of the mass servo system in terms of the actuator bandwidth. One has to note, that this last assumption actually favors the classical rotor speed approach, since the time constant of IC engines is relatively slow w.r.t. DC motor servo control.

Finally, we present the Bode diagram of (38) and (48) in Fig. 4. In the same figure we add the Bode diagram of the moving mass control concept with the mass dynamics presented by a PT_1 term, with time constant equal the rotor time constant T_r. From the presented curves one can conclude that the system with the moving mass control has a higher crossover frequency ($\omega_{c,mm}$) than the system with a traditional control concept ($\omega_{c,r}$). In particular, from Fig. 4 we get:

$$\begin{aligned} \omega_{c,mm} &= 2.68 \text{ rad/s} \\ \omega_{c,r} &= 0.12 \text{ rad/s}. \end{aligned} \tag{49}$$

This last result is a consequence of the higher open loop gain in (38) than in (48), and it implies that the moving mass control concept has a theoretically faster dynamics than the traditional rotor control. One could even use a much slower, and thus a cheaper, MMC servo system to control the attitude with the similar bandwidth as in the common rotors approach.

Comparing PT_2S vs PT_1 servo model, we conclude that there is no significant difference in crossover frequencies, but the biggest difference is in the system gain margin. With PT_1 model we theoretically achieve infinite gain margin, but for a PT_2S term we get a finite gain margin value. Furthermore, the system phase margin is reduced when analyzing servo dynamics as PT_2S term. These observations justify the introduction of the second order model for the mass servo system, which allows us to determine more realistic boundaries of the system stability.

The biggest shortcoming of the MMC is the maximum pitching (rolling) moment that can be generated

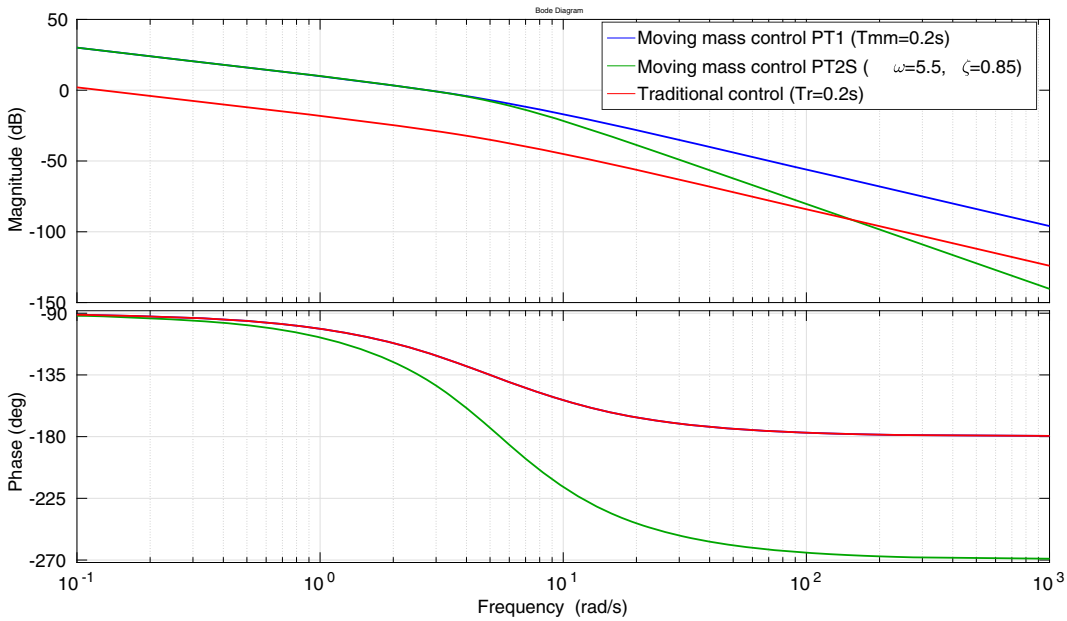

Fig. 4 Bode diagram of the open loop systems. The first system is controlled through the moving mass control (blue and green curves) and the second through variations in rotor velocities (red curve)

with such a concept, due to the physical limitations on the mass maximum displacement. Therefore, previous analysis is valid only for mass displacements that do not violate saturation limits. The maximum moment of our concept is discussed in the next section, with a goal to find parameters of mass weight and maximum displacement reach that provide the maximum dynamic torque.

4 Mechanical Parameter Design

In this section we present the design analysis for important parameters of the MMC control, namely the weight of the moving mass, its maximum displacement reach, its vertical position w.r.t. the CoG and its dynamics. We aim to find parameters that provide the highest dynamic torque and low sensitivity to model variations.

4.1 Design of Mass Weight and Arm Length

We start by analyzing the influence of moving mass weight and its maximum displacement on attitude dynamics. We assume that the initial mass position is in the half of the motor arm, and therefore maximum displacement of the mass equals $D = \pm\frac{L}{2}$, where L is the motor arm length.

The goal of this analysis is to optimize the angular speed response. In other words, we define a metric which reflects the bandwidth of the open loop, and optimize the metric w.r.t. the moving mass weight and motor arm length. As an appropriate metric we propose to use the maximum angular acceleration that can be achieved for the given set of parameters.

The measure of the maximum angular velocity can be expressed from (38):

$$\dot{\omega}_y = \frac{2mgx}{I_{yy}}, \tag{50}$$

where we used $x = x_1 = x_3$ as mass 1 and 3 longitudinal displacement in the x-direction of the quadrotor frame. Note that (50) corresponds to the steady state value of the angular acceleration given the step reference to the mass 1 and 3 position:

$$\dot{\omega_y}(\infty) = \lim_{s\to 0} s \cdot G_{\dot{\omega}_y}(s) \cdot U(s) = \frac{2mgx}{I_{yy}}. \tag{51}$$

The model of the pitching MoI for the overall system is given as:

$$I_{yy} = I_{b,yy} + \sum_{j=1}^{4} \left(I_{maj,yy} + I_{mj,yy}\right) \tag{52}$$

where $I_{b,yy}$ is the MoI of the quadrotor rigid body parts, which does not depend on moving mass position nor motor arm length. These parts include central body, landing gear and gas motors. $I_{maj,yy}$ and $I_{mj,yy}$ are the moments of inertia of the motor arms and moving masses, which depend on the variables that we want to optimize. Note that we assume that the positions of the gas motors are fixed, and consequently their MoIs do not change with the change of motor arm length. Therefore, we consider extending motor arms only to achieve an extension of the moving mass rail, i.e. the mass maximum displacement. We get the value for $I_{b,yy}$ from our initial CAD design.

To determine motor arms inertial properties, we model an arm as a hollow square tube made of carbon fibre and we express the MoI as a function of its length. Based on known formulas for inertial properties of a hollow tube and utilizing initial arm CAD design, we determined the following relation:

$$\begin{aligned} I_{ma2,yy} &= I_{ma4,yy} = \kappa_1 \cdot L \\ \kappa_1 &= 0.1404, \end{aligned} \tag{53}$$

where $I_{ma2,yy}$ and $I_{ma4,yy}$ denote the pitching moments of inertia of arms 2 and 4 w.r.t. the vehicle CoG.

Similar procedure, applied to determine the pitching MoI of the longitudinal motor arms (x-direction), yields:

$$\begin{aligned} I_{ma1,yy} &= I_{ma3,yy} = \lambda_3 \cdot L^3 + \lambda_1 \cdot L \\ \lambda_3 &= 2.0159\ ,\ \lambda_1 = 0.0702. \end{aligned} \tag{54}$$

where $I_{ma1,yy}$ and $I_{ma3,yy}$ denote the pitching moments of inertia of arms 1 and 3 w.r.t. the vehicle CoG.

In this analysis a moving mass is modeled as a point mass. Therefore, the mass 2 and 4, that are placed in the lateral direction and perfectly aligned with the body y-axis, do not contribute to the pitching MoI.

On the other hand, the MoI of the mass 1 and 3, can be expressed as (their vertical displacement is neglected):

$$I_{m1,yy} = m\left(\frac{L}{2} + (1-2\mu)x\right)^2$$
$$I_{m3,yy} = m\left(\frac{-L}{2} + (1-2\mu)x\right)^2. \quad (55)$$

From (55), the MoI of moving masses depends on the mass position x, and therefore it will change during the mass control. In this analysis we propose to use the maximum value of the term $I_{m1,yy} + I_{m3,yy}$. It can be easily shown that this maximum value is achieved for $x = \pm\frac{L}{2}$, which corresponds to the maximum mass displacement. Letting $x = \frac{L}{2}$, we get the following expression:

$$\dot{\omega}_y = \frac{mgL}{I_{b,yy} + 2I_{ma1,yy} + 2I_{ma2,yy} + I_{m1,yy} + I_{m3,yy}}. \quad (56)$$

We depict (56) as a 3D surface plot in Fig. 5. To get the maximum angular acceleration, we seek for an extremum of (56), as a function of two variables, m and L. Taking the first and second derivatives of (56), we do not get candidates for extremum points. However, fixing m and taking the derivative w.r.t. L, we get the expression for L_e that gives maximum angular acceleration for provided m. As L_e is the solution of a cubic polynomial, which is not a compact expression, we do not present it here.

Presented results suggest that, in order to get better dynamical performance, one should increase m indefinitely. In practice, the moving mass weight is limited by the vehicle payload, and we certainly do not want to spend all the available payload on moving masses only. Therefore, design strategy is to choose the moving mass weight according to the given payload requirements and then compute optimal motor arm length. According to the datasheet of the gas motor and rotor that we plan to use, the maximum thrust of a single rotor is approximately 20 kg [18]. Based on our experience, we decide that the mass of the moving mass should not exceed 10% of the maximum thrust of a single rotor, which yields $m_{max} = 2$ kg. At this point we choose $m = 1$ kg and from Fig. 5, we get $L_e = 0.84$ m for the chosen m. Given $(m, L) = (1, 0.84)$, (56) yields:

$$\dot{w}_{y,max} = 0.93 \text{ rad/s}^2. \quad (57)$$

The arm length of the vehicle presented in Section 6 is almost identical to the optimal value computed in this Section. The biggest difference between the analyzed system and designed vehicle is the length of the moving mass path. In this analysis we assumed that the moving mass path length is equal to the arm length. However, due to the physical dimensions of the designed moving masses and central UAV body, the actual path length is limited to 50 cm. The final CAD designs of the UAV arm and moving mechanism are shown in Fig. 6a.

4.2 Moving Mass Dynamics Design

In this analysis we aim to determine the required speed-torque curve for the servo system driving a moving mass. The determined curve plays a crucial role for choosing the appropriate servo drive. Our approach is to determine the required dynamics for the

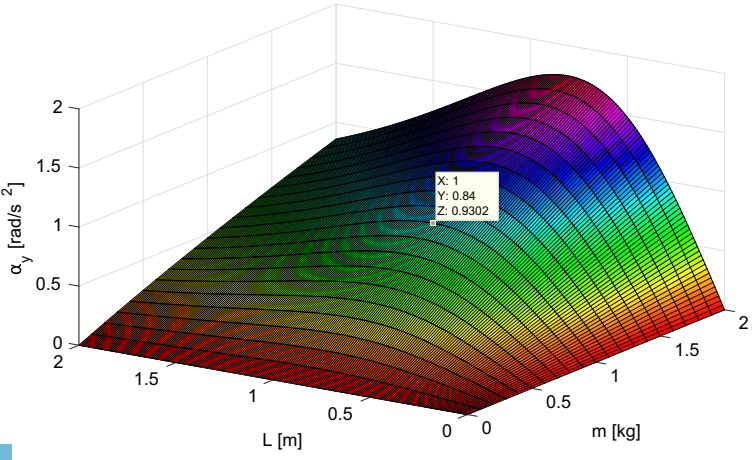

Fig. 5 Maximum angular acceleration as a function of the mass weight and arm length. The marked point on the surface corresponds to the chosen value of parameters $(m, L_e) = (1, 0.84)$.

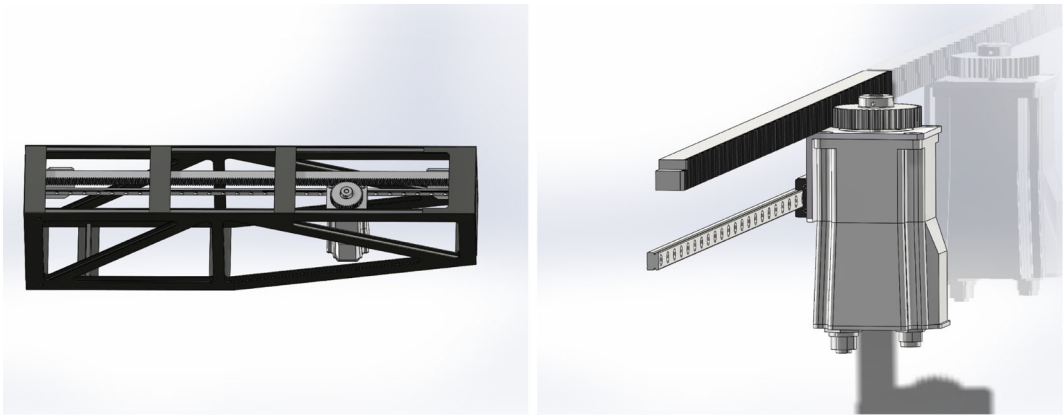

(a) Arm with the moving mass mechanism. (b) Isolated moving mass mechanism.

Fig. 6 CAD designs of the UAV arm and moving mass mechanism

moving mass which stabilizes the vehicle and achieves desired robust performance. Given the determined dynamics, we compute accelerations and velocities exhibited by the moving mass given a step setpoint on its position. To transform these linear quantities to their angular counterparts exhibited by the motor, a transmission mechanism, which translates the angular motion of the motor to the linear motion of the moving mass, is required. We have chosen a rack and pinion mechanism where the motor, mounted on a linear guide, acts as the moving mass (see Fig. 6). For this design, the radius of the gear determines the relation between linear and angular velocities/accelerations.

First, we analyze the influence of the moving mass dynamics to system stability and robustness. In particular, we compute gain margin, phase margin and crossover frequency of the transfer function (38) as a function of the moving mass natural frequency ω_{mm}. From these characteristics we determine natural frequency required to achieve desired robustness and speed of the closed loop response [19]. Damping factor in (29) is another parameter that determines the dynamics of the servo system. However, through the analysis we have concluded that for the damping factors greater than 0.6, there is no significant difference in the analyzed frequency characteristics. Therefore, we choose damping factor 0.7 (technical optimum) and vary the natural frequency in the interval [1,50] rad/s. In addition, we vary also moment of inertia value in range [2–10] kgm^2 to account for uncertainty of this parameter. The computed characteristics are depicted in Fig. 7.

From Fig. 7a and b one can conclude that both gain and phase margin increase as the moving mass dynamics gets faster (i.e. ω_{mm} increases). For the chosen natural frequency, the system with bigger inertia has greater gain and phase margin than the system with smaller inertia. Interesting result is obtained from Fig. 7c. The system crossover frequency increases with an increase in the moving mass natural frequency, but only up to a limit value. This limit value is determined by the moment of inertia and it increases as the moment of inertia decreases.

Finally, we utilize practical recommendations on gain and phase margins from [19] in order to obtain a reasonably robust system. In particular, the recommended upper limit of the gain margin is 5, while the upper limit of phase margin is 60°. For these values and the moment of inertia 6 kgm^2 (mid value of the analyzed range), we obtain that the natural frequency should be at least 12 rad/s.

From the determined parameters of the moving mass transfer function (29), we compute the velocities and accelerations exhibited by the mass given a step setpoint 0.25 m (half of the mass maximum displacement). These responses are shown in Fig. 8. The torque of the servo motor (τ_{sm}) required to accelerate/decelerate the moving mass and its rotational speed (Ω_{sm}) are computed as follows:

$$\tau_{sm}(t) = ma_{0,i}(t)r, \tag{58}$$

$$\Omega_{sm}(t) = \frac{v_{0,i}(t)}{r}, \tag{59}$$

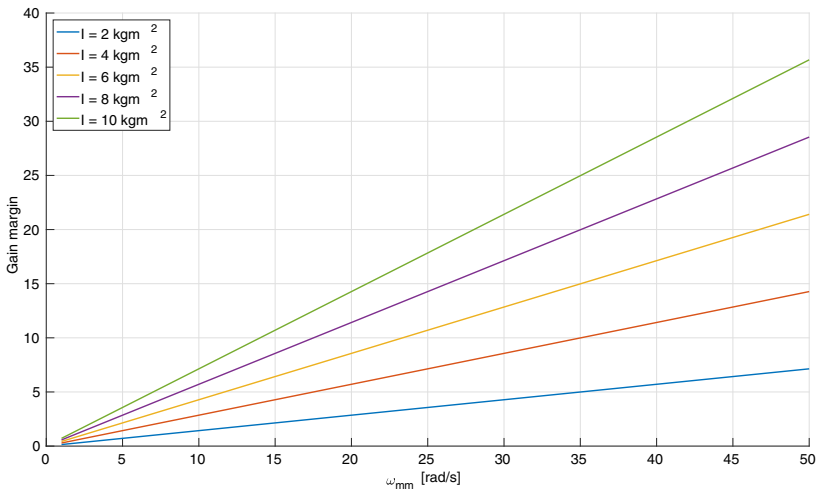

(a) Gain margin

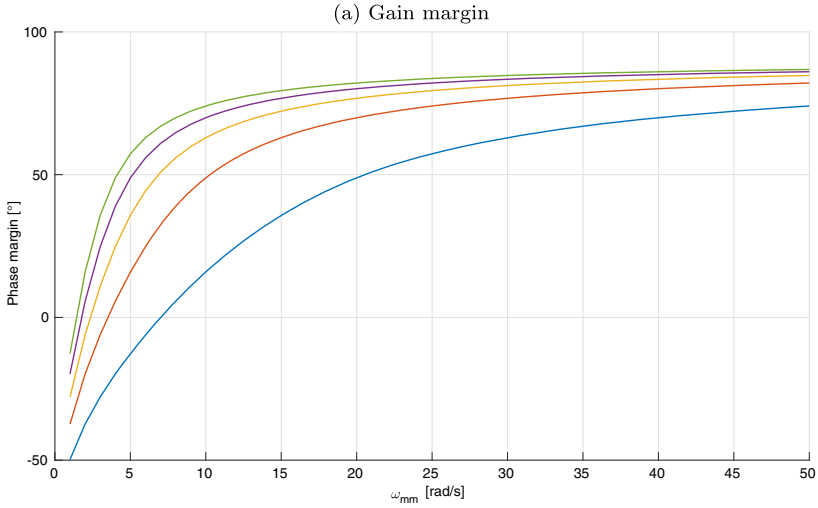

(b) Phase margin

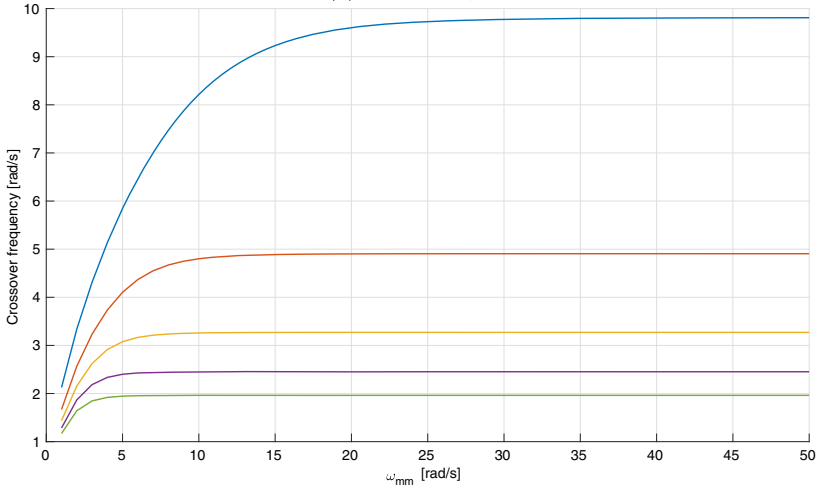

(c) Crossover frequency

Fig. 7 Frequency analysis of attitude dynamics as a function of the moving mass natural frequency

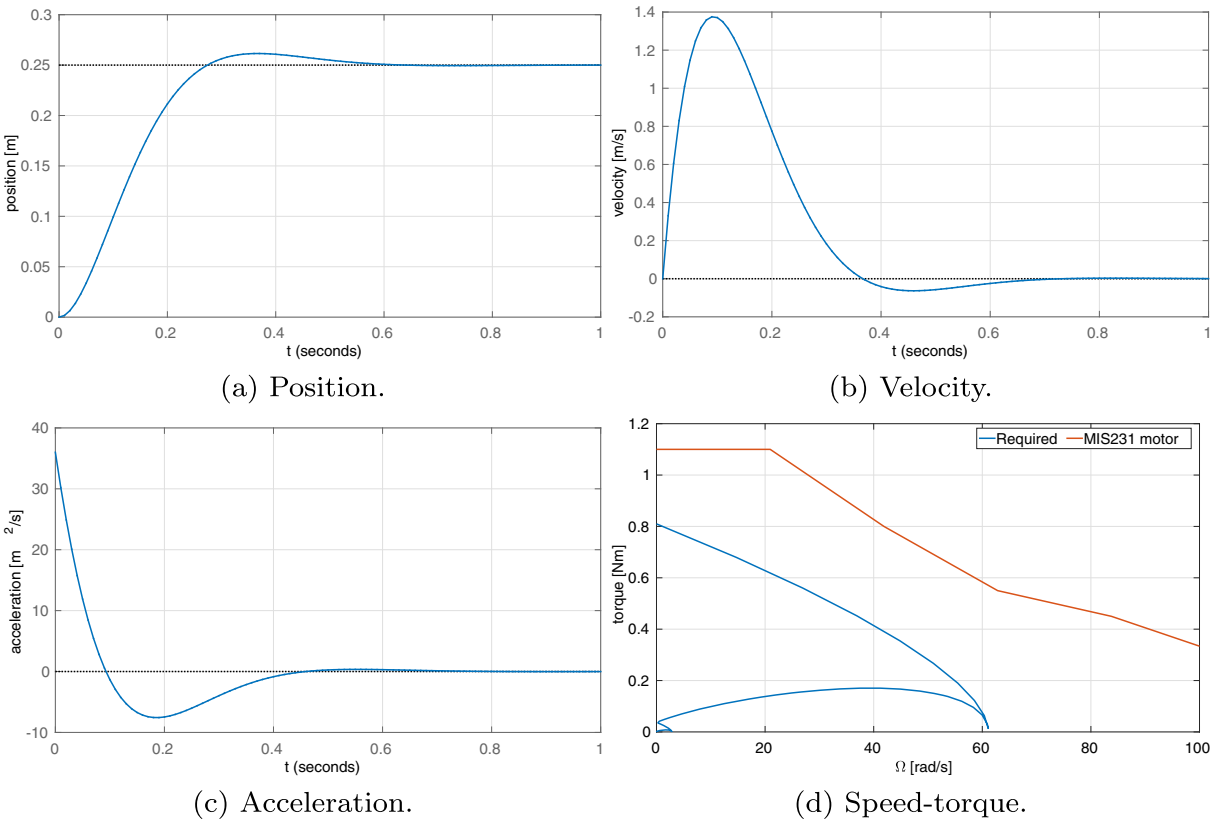

(a) Position. (b) Velocity.

(c) Acceleration. (d) Speed-torque.

Fig. 8 Designed responses of the moving mass position, velocity and acceleration. In (d) we show speed-torque curve required for a servo system driving the moving mass. In the same figure we show the speed-torque curve of the chosen servo motor

where $a_{0,i}$ is the moving mass acceleration and $r = 0.045$ m is the gear radius.

For each time instant we acquire a pair of speed and torque values computed by (58) and (59). The set of these values presents the required speed-torque curve for the servo system, shown in Fig. 8d. When choosing the servo drive, we have considered using DC, BLDC and stepper motors. Eventually, stepper motors turned out to be the most appropriate for our application. In particular we have chosen JVL MIS231 stepper motor with integrated driver and control board. The speed-torque curve of the chosen motor is shown in Fig. 8d, which proves its fit for the considered design.

4.3 Mass Vertical Displacement Considerations

In this section we analyze the influence of the mass plane vertical displacement w.r.t. the vehicle CoG. In our recent work we have used the Hurwitz criterion to show that the angular rate loop of the continuous system, closed with P controller, can become unstable in the case where the mass plane is above the CoG (i.e. $z_m > 0$). The same does not hold for $z_m < 0$, for which linearized continuous time system is stable for every gain. For $z_m = 0$ the vehicle model is qualitatively similar to the model of a standard quadrotor which uses variations in rotor velocities to control the attitude [14]. In this work we analyze in more details the attitude dynamics when z_m crosses from negative to positive values.

First, we analyze the sensitivity of the system to the z_m parameter [19]. To that end, we derive the relative sensitivity of the system to variations in z_m:

$$S_z(s) = \frac{\partial \ln G_\omega}{\partial \ln z_m} = \frac{z_m}{G_\omega}\frac{\partial G_\omega}{\partial z_m} = \frac{-(1-4\mu)z_m s^2}{g-(1-4\mu)z_m s^2} \tag{60}$$

Note that the system sensitivity does not depend on the moving mass dynamics. Therefore, (60) is valid for both PT_1 model of the moving mass dynamics [15]

and PT_2S model used in this paper. Using ZOH transformation with sampling time $T_s = 0.01\ s$, (60) is transfered to discrete domain. For the discrete sensitivity function, magnitudes of Bode diagrams, for several positive and negative z_m values, are shown in Fig. 9. We conclude that the sensitivity of the system is significantly different for positive and negative z_m and the system is more sensitive for negative values of z_m. For $z_m = 0$, an ideal case difficult to achieve in practice, the system sensitivity is 0. The sensitivity peaks for negative z_m occur at the frequencies of the system zeros. Those frequencies can be derived from (60).

Next, we show how the dynamics of the closed loop angular rate changes with the variations of z_m. To that end, we give a root locus analysis for the discrete system (39). First, in Fig. 10 the root locus curve for z_m in range $[-0.2, -0.01]$ is given. Two curves start at the poles of the open loop system and finish up at two zeros. We notice that the closed loop can become unstable for sufficiently large gain, which, as already stated, is not the case if continuous system is analyzed [14]. Therefore, this property is a consequence of discretization and should be taken into considerations in the controller design.

In Fig. 11 we show the root locus for $z_m = 0$. In this case, there are no zeros in the open loop of the continuous system and two zeros occur in the closed loop as a consequence of discretization.

The third type of the root locus curve is given in Fig. 12 for z_m in range $[0.01, 0.2]$. Again, there is a gain limit that guarantees the system stability, which is qualitatively similar to the continuous time system, analyzed in [14]. Furthermore, as z_m increases, the zeros of the open loop are getting closer to the critical point (1,0), thus reducing system stability margin and bandwidth.

To further demonstrate how z_m parameter effects vehicle dynamics, we show step response of the angular velocity loop controlled with a simple P controller. We choose controller gain $K_p = 1.5$, designed for the system with $z_m = 0$, for which we get a smooth response with a small overshoot. We simulate the system with the same controller for z_m values -0.2 and 0.2 m. Step responses for these cases are shown in Fig. 13. The system with negative z_m remains stable, while the system with positive z_m exhibits oscillations, suggesting that using the gain chosen for $z_m = 0$ we have reached system stability boundary. Further increase in z_m, which could happen if the vehicle grabs an object, would further destabilize the system. Therefore, one has to be careful when designing controller gains for this system, particularly for applications including object transportation and manipulation. Furthermore, we observe from the given responses a non-minimum phase behavior of the system with $z_m > 0$, where the vehicle starts rotating in the direction opposite to the given reference before eventually reaching the desired state. For $z_m < 0$ the opposite effect happens: The system zeros accelerate the vehicle towards the given reference for a short period in which they dominate the dynamics.

The vertical displacement of the moving masses used in the experimental testbed (Section 6) is slightly above the vehicle CoG. Ideally, we would choose $z_m = 0$, which would make the control of the system virtually identical to the control of a common quadrotor. However, in practice it is extremely difficult to achieve exactly $z_m = 0$ and we can expect variation of

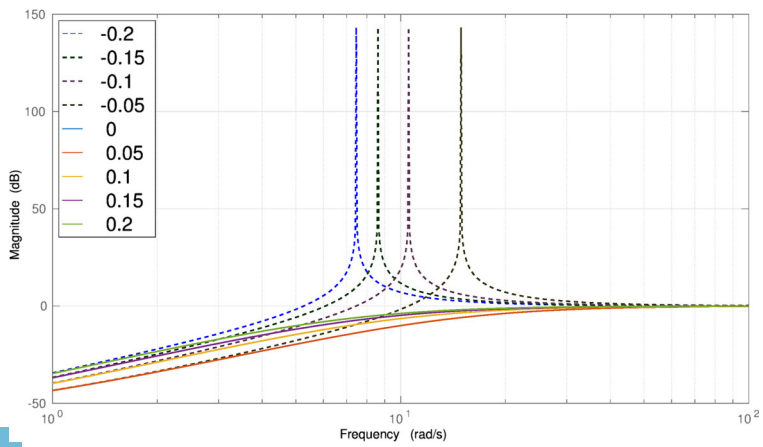

Fig. 9 Sensitivity of the system (open loop) to variations in z_m

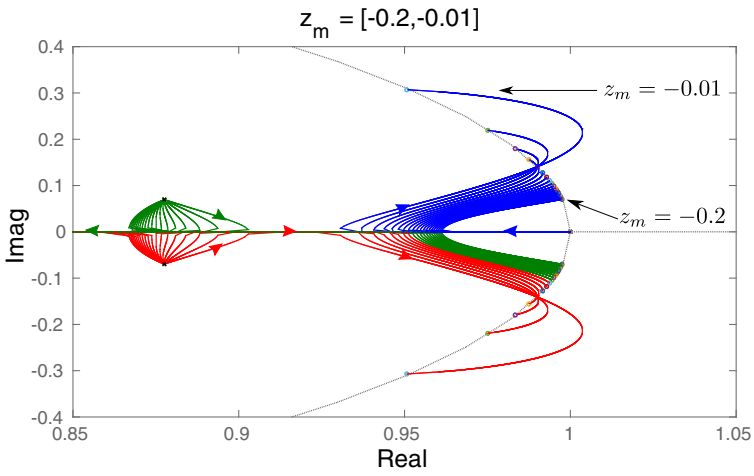

Fig. 10 Root locus curve for negative z_m

CoG by adding equipment (e.g. gimbal with a camera) or carrying an object. In each case, the analysis given in this section provides valuable insights into system dynamics and we use it to determine the controller gains for both simulation and experimental testbed. In the remainder of this paper we work with $z_m = 0.05$ m, which corresponds to the mass vertical displacement in the full scale vehicle that we have recently built.

5 Simulation Results of the Free-flight Quadrotor Control

We have developed a vehicle model in the Gazebo simulator within Robot Operating System (ROS). We use this Gazebo model to verify the mathematical model presented in Section 2 and to test the devised control algorithms in a realistic simulation environment. This model is based on two ROS packages widely used for simulating rotor-UAVs, namely *hector_gazebo_plugings* [20] and *rotors_simulator* package [21]. As any Gazebo model, it consists of several links connected with joints. There is a central body link to which the motor arms are attached. At the end of a motor arm, there is a rotating joint to which a rotor is attached. To simulate rotor dynamics, we utilize a plugin from the *rotors_simulator* package. We extend this standard quadrotor model by adding a prismatic joint in each motor arm, used to move a cuboid link with inertial properties within the arm. Throughout this paper this cuboid link is called the moving mass. A PID plugin in *ros_control* package is utilized to control the moving mass position. Finally, two

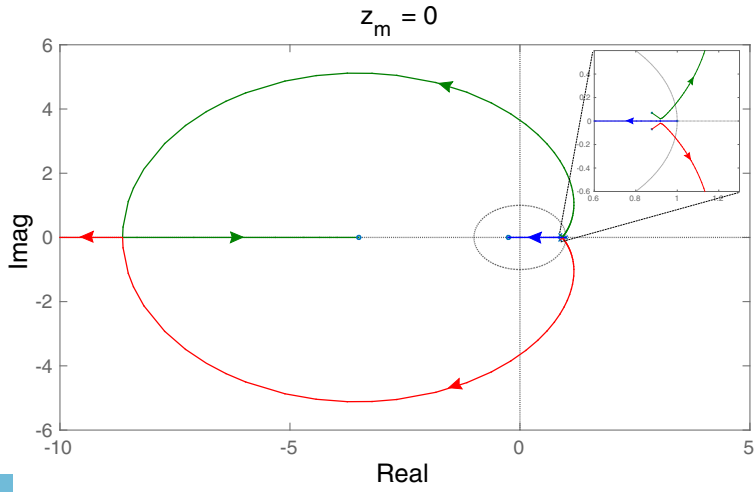

Fig. 11 Root locus curve for small positive z_m. On the curve for $z_m = 0.05$ m, we mark the point which corresponds to the designed gain of the angular rate loop

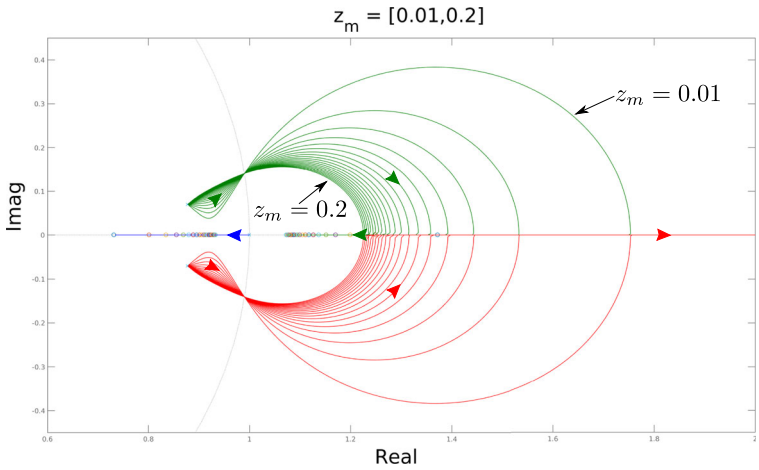

Fig. 12 Root locus curve for positive z_m

plugins from *hector_gazebo* package are used to simulate realistic sensory set consisted of an inertial measurement unit and a generic pose sensor. We use fusion algorithms developed in our previous work to estimate 6 DOF vehicle pose [22, 23].

An important note to the Gazebo model presented in this paper. We consider gas motor dynamics to be similar to the dynamics of an electrical motor with a large inertia. In other words, a change of the gas motor rotational speed, i.e. a change of the rotor speed, is approximated with a PT1 dynamics with 200 ms time constant. As a comparison, time constant of brushless DC motors, dominantly used in rotor-UAVs, range from 15 to 50 ms. More comprehensive gas motor dynamics will be investigated in our future work. The complete source code used throughout simulation experiments can be found in [24].

5.1 Controller Design

In this paper we consider controller design in discrete domain. For the height and yaw control we use PID

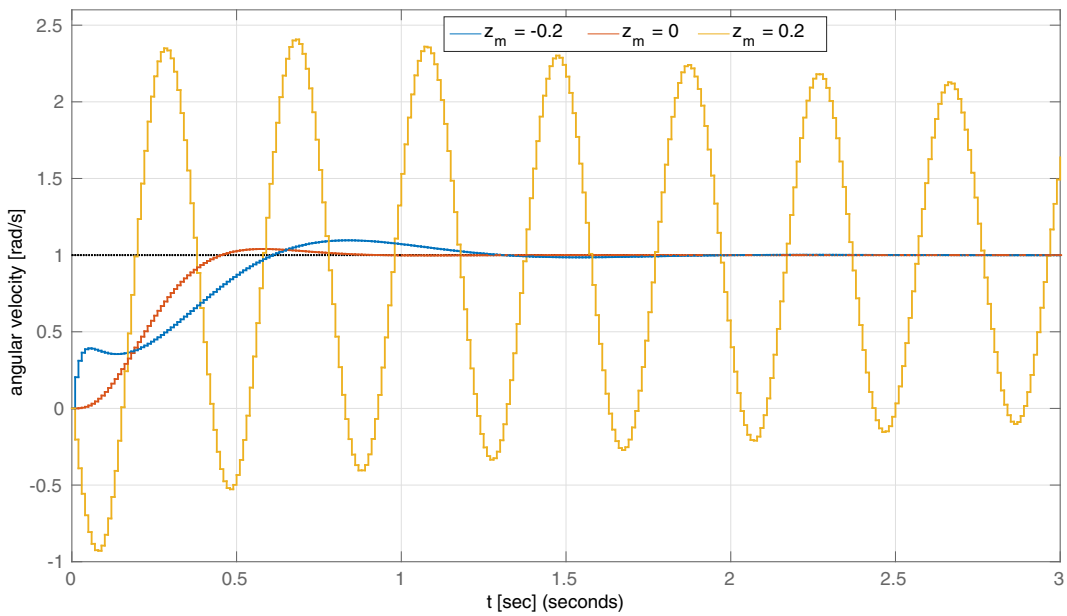

Fig. 13 Step responses of the angular velocity loop controlled with P controller. The controller gain is designed for $z_m = 0$ and we test the response of the systems with $z_m = -0.2$ m and $z_m = 0.2$ m

cascade control algorithms, whose design follows a standard procedure already presented in our previous work [22, 23], and will not be discussed here.

For the pitch (roll) control, we design a classical cascade control, with P controllers in the inner (angular rate) and outer loop (angle). To address both stability and performance of the system, we choose root locus design. The root locus curve for $z_m = 0.05$ m, representing angular velocity closed loop, is shown in Fig. 14a. We choose $Kp_{in} = 0.7$ which gives a pair of complex-conjugate poles and a single real pole.

For the outer loop, first we determine the transfer function of the open loop system which includes the designed closed loop angular rate dynamics and an integrator:

$$\frac{\theta(s)}{\dot{\theta}_{ref}(s)} = \frac{-0.0002364z^2 + 0.0004782z - 0.0002365}{z^4 - 3.748z^3 + 5.268z^2 - 3.293z + 0.7727}. \tag{61}$$

The root locus curve for (61) is given in Fig. 14b. We choose $Kp_{out} = 1.4$ as the gain for the outer P controller, which gives two pairs of complex-conjugate poles with satisfactory speed and damping. Note that the choice of poles for the case where we model the mass servo system with PT_2S term is more complicated than in the case where a PT_1 term is used [15]. Therefore we use an iterative procedure: Once the poles are chosen, we analyze the step response of the closed loop, and if the speed or damping were not satisfactory, we pick another set of poles from the root locus curves.

5.2 Simulation Results

The system and controller have been thoroughly tested in the Gazebo environment. First, we present the response of the system given the step reference on roll and pitch angles. The results are shown in Fig. 15. In addition, we give the response of the mass servo system (one for each mass) responsible for shifting the CoG (Fig. 16). The system follows the reference with rising time approximately 1 s. There is no significant difference in roll and pitch dynamics and coupling between roll and pitch is as well not observed. One can notice a small influence of the non-minimum phase zero - the vehicle starts rotating in the direction opposite to the given reference before eventually reaching the desired state.

Finally, we test the stability margin of the vehicle. To that end, we increase the proportional gain of the outer pitch loop until the stability margin is reached. The gain is increased by 1 every 10 s. The response of the pitch is shown in Fig. 17. The critical gain equals approximately 7.5. For that gain, the vehicle remains airborne, but exhibits high frequency oscillations due to the saturation limits on mass positions (see Fig. 18). The theoretical critical gain, determined from root locus in Fig. 14b, equals 8.2, which suggests a satisfactory agreement between a linearized model used for root locus analysis and the nonlinear Gazebo model. The video showing simulation experiments can be found in [25].

6 Experimental Results on the Laboratory Testbed

For the experimental testbed we use a full scale vehicle mounted on a gimbal (Fig. 19) whose motion is constrained to 2DOF (roll and pitch angle). To satisfy conditions (45) for gimbal dynamics, we have mounted the axes of rotation as close as possible to the vehicle CoG. While in [15] we used a small scale gimbal with Dynamixel motors as a mass servo system, the full scale vehicle uses MIS231 stepper motors with a rack and pinion mechanism transforming rotational to linear motion. A Pixhawk flight controller is attached to the vehicle main body and we utilize its IMU to measure attitude. All control and estimation algorithms have been implemented onboard Pixhawk which ensures real-time execution. The description of the complete vehicle's hardware and software infrastructure is beyond the scope of this paper and will be addressed in our future work. In the remainder of this section we present identification procedures used to determine important system parameters and experimental results on roll/pitch control.

6.1 Identification Results

We have conducted experiments in order to identify important parameters for system dynamics, namely moment of inertia and moving mass dynamics. For the moment of inertia identification, the vehicle is excited with a known constant torque, independently

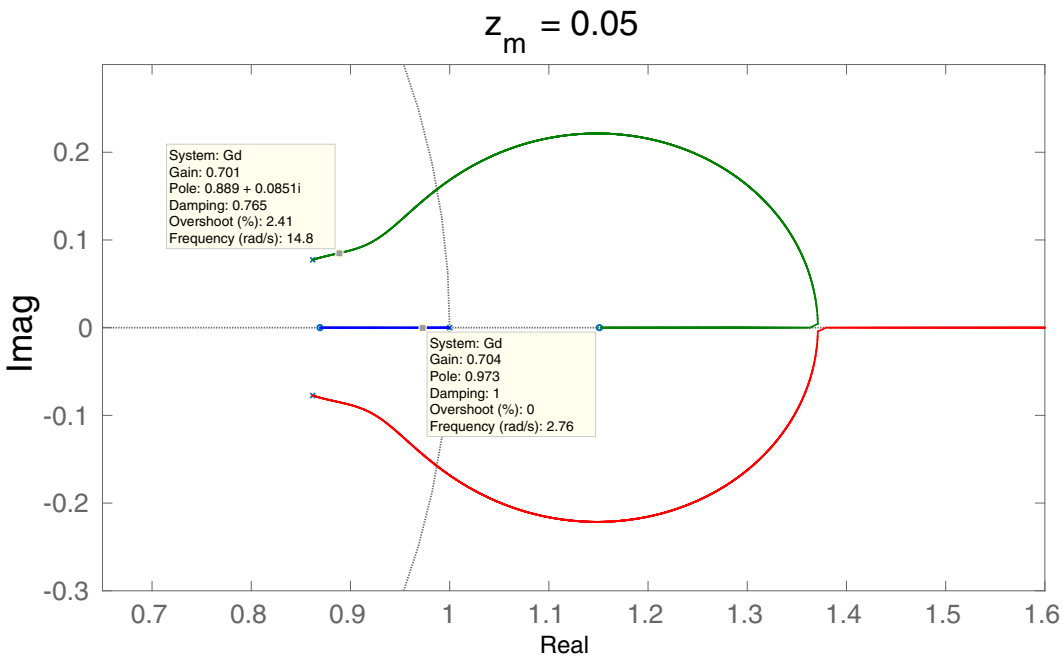

(a) Root locus curve for the inner control loop (angular velocity).

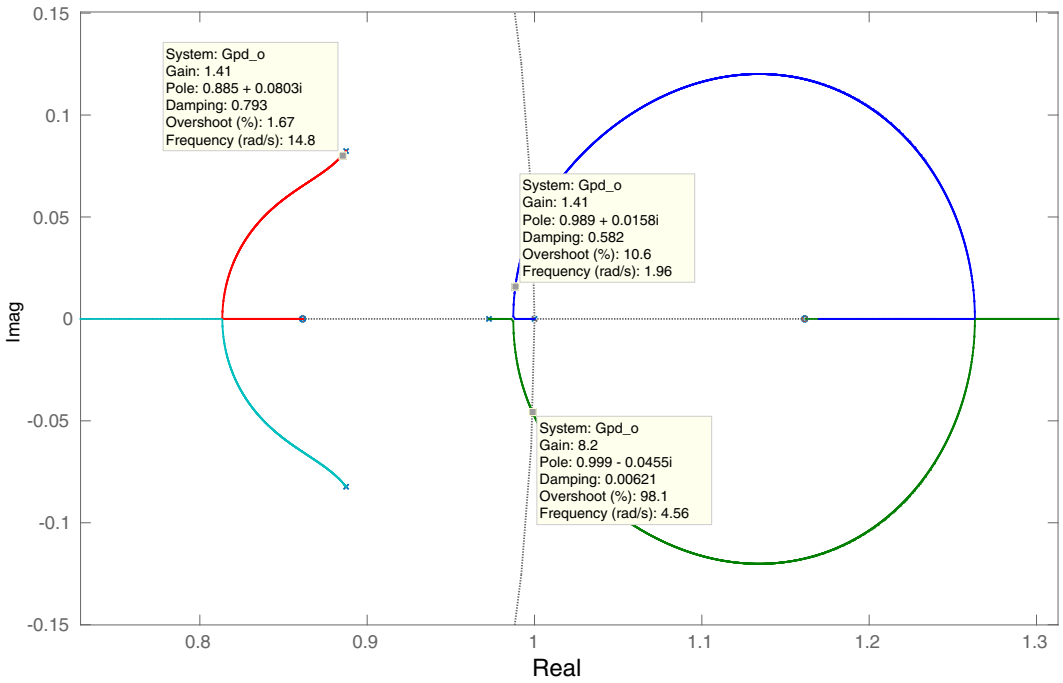

(b) Root locus curve for the outer control loop (angle).

Fig. 14 Root locus curves used for the design of the proportional cascade controllers

for roll and pitch axis. To produce constant torque, we utilized existing moving mass mechanisms: The masses are maximally displaced and the vehicle is released to freely rotate from the initial position ($\phi_0, \theta_0 = 0°$). Since the masses do not move and the torque is constant, it follows from (38) that the pitch

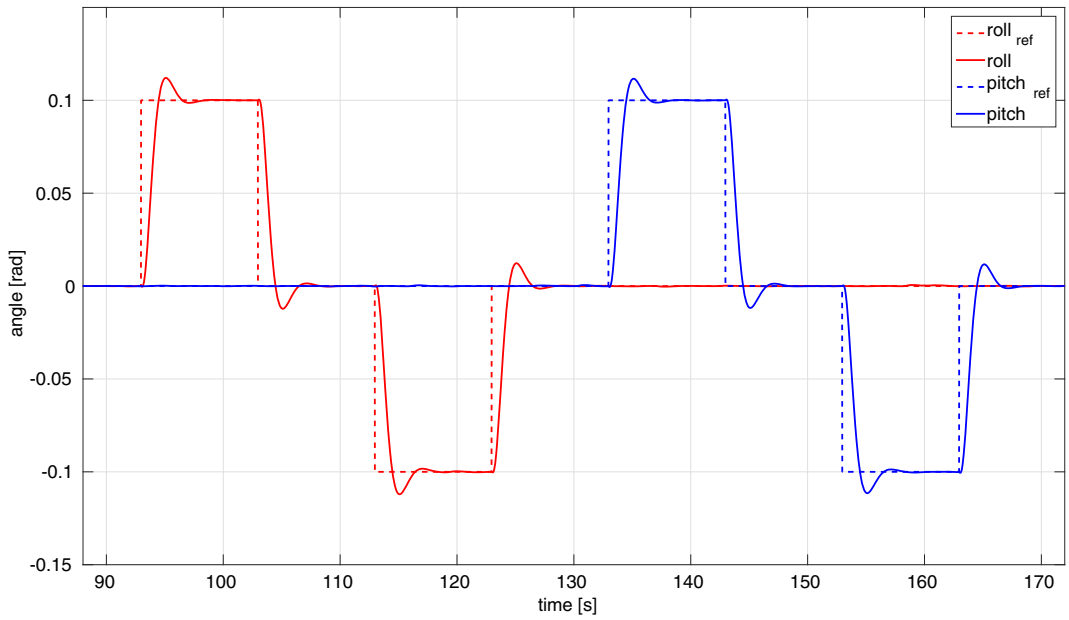

Fig. 15 Gazebo model simulation results. Here we show a sequence of roll and pitch references and the corresponding responses

dynamics for this case can be described by double integrators:

$$\frac{\theta(s)}{\tau(s)} = \frac{1}{I_{yy}s^2}, \tag{62}$$

where $\tau(s) = \frac{2mg\Delta l}{s}$ and $\Delta l = 0.25$ m as the mass maximum displacement.

We have conducted the described experiment for several times to obtain bigger identification dataset.

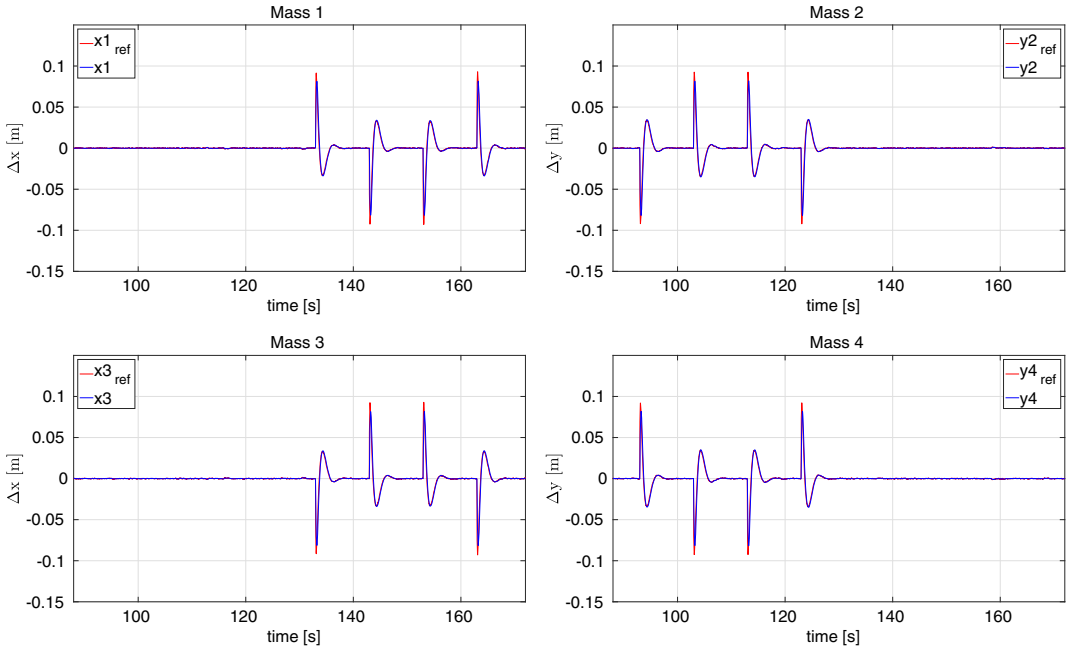

Fig. 16 Simulation responses of the moving masses position for a sequence of attitude references shown in Fig. 15

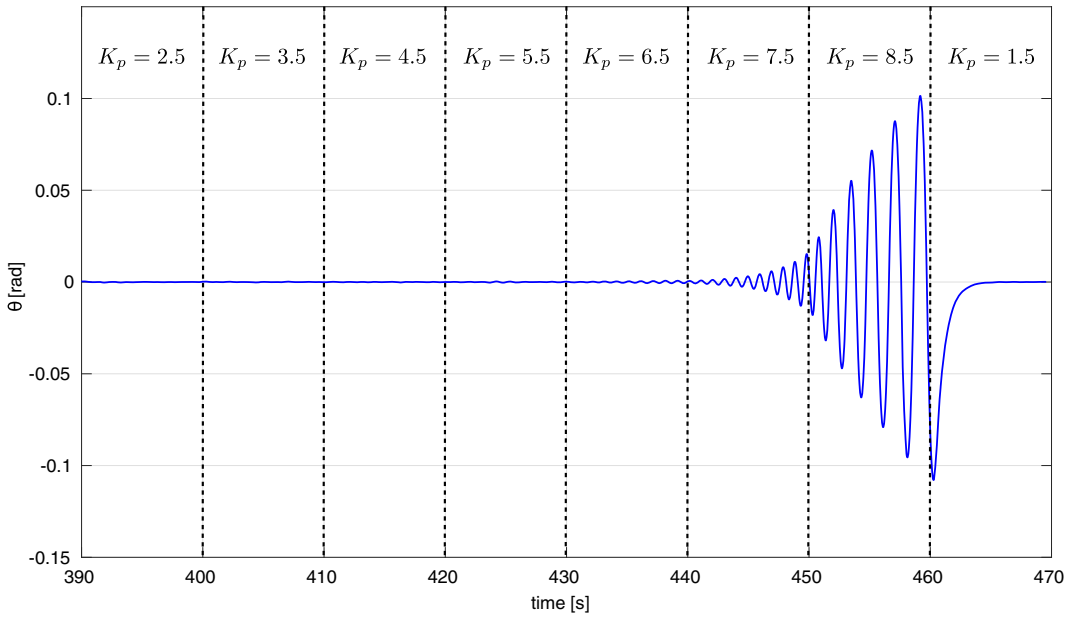

Fig. 17 Gazebo model simulation results on stability. The controller gain is increased until the stability margin is reached

To find the moment of inertia value, we have run an optimization procedure in MATLAB® based on the *fminsearch* function. The optimization criteria is chosen as the minimum root mean square (RMS) error between the measured response and response predicted with (62), computed on each dataset. The same procedure is repeated for roll axis. Eventually, we have obtained the following values $I_{xx} = 6.8$ kgm^2 and

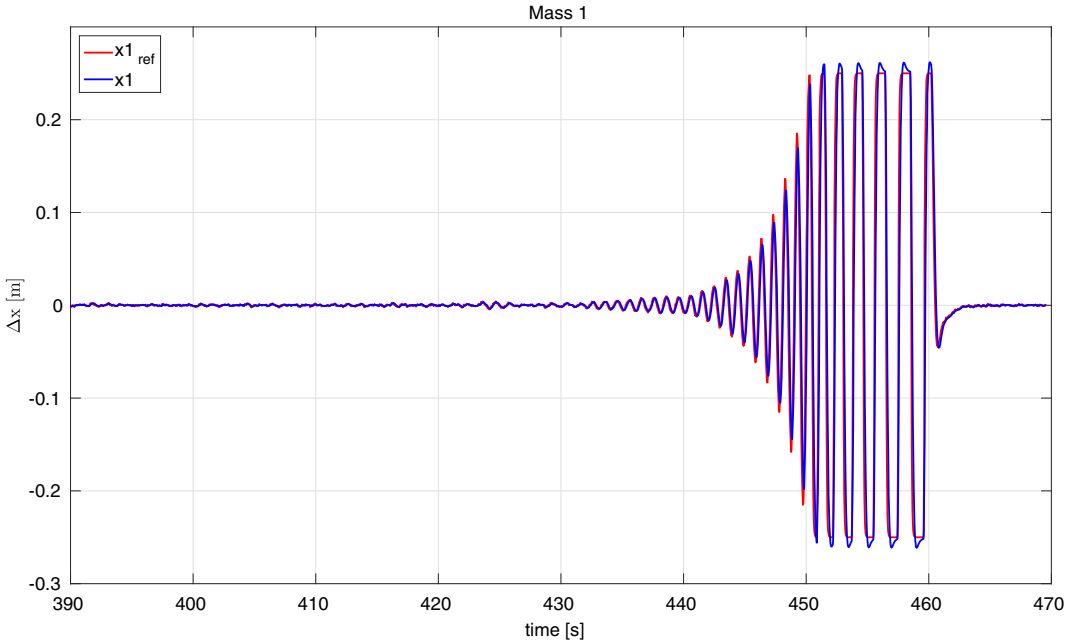

Fig. 18 Position responses of mass 1 during the stability test

$I_{yy} = 6.5$ kgm^2. The measured and identified angle responses are shown in Fig. 20.

Next, we have conducted experiments to identify the moving mass dynamics. To that end, a step position setpoint is given to the moving mass and its response is measured. Again, we utilize MATLAB® and its System Identification Toolbox™ to determine the moving mass transfer function. Eventually, the best fit (the minimum RMS error between the measured and predicted response) is achieved with PT_2S term with the following parameters $\omega_{mm} = 17$ rad/s and $\zeta_{mm} = 0.85$. Note that the identified natural frequency is higher than the minimum required frequency ($\omega_{min} = 12$ rad/s) computed in Section 4, from which we conclude that the chosen moving mass system should be able to stabilize vehicle's roll and pitch angles. The measured and identified position responses are given in Fig. 21.

Finally, we have also determined the weight of each moving mass ($m = 1\ kg$) and entire vehicle ($M = 34\ kg$) using a laboratory scale.

6.2 Control Results

We have started the experiments with the same controllers structure and gains as in the simulation. These controllers were able to stabilize the vehicle but we noticed two issues, which were not observed in simulation. First, the response of the angle closed loop contained a static error, which is mainly due to the friction and a small displacement of the gimbal axes from the vehicle CoG. Therefore, we added integral component in the outer (angle) control loop with gain $K_{i,out} = 1$. One can easily prove, using results from [14], that the system with PI-P cascade controllers is stable. Second, there was a significant noise in angular

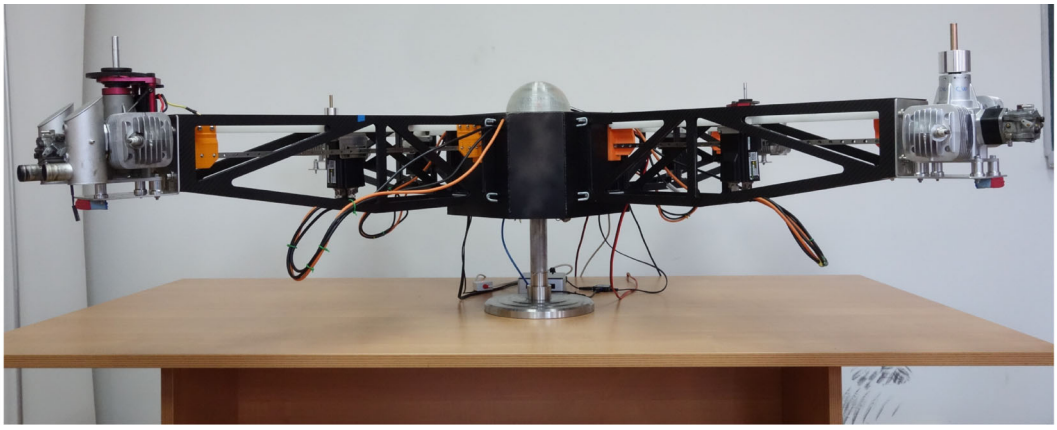

(a) The UAV mounted on a gimbal.

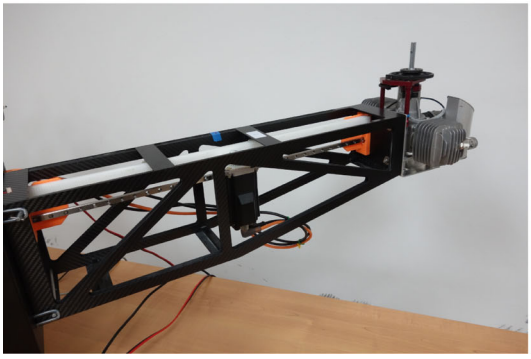

(b) Vehicle arm.

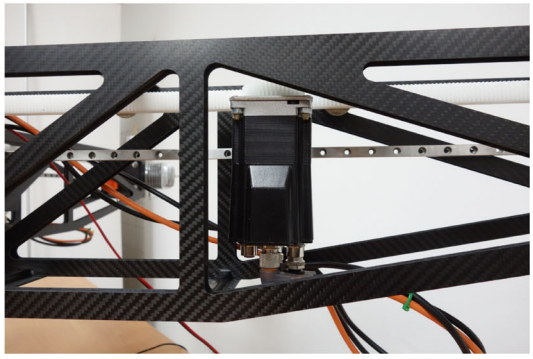

(c) Moving mass.

Fig. 19 Laboratory testbed - the UAV mounted on a gimbal and constrained to 2DOF (roll and pitch angle). Four stepper motors are used to move masses. Showing also a DLE111, an internal combustion engine which will be used to power the propulsion system

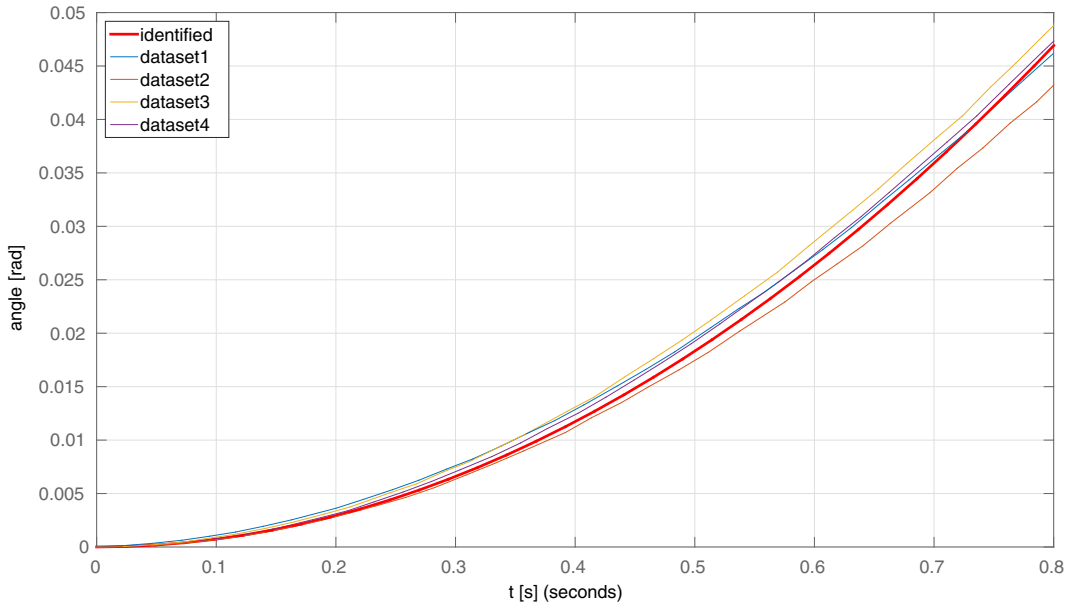

(a) Roll axis.

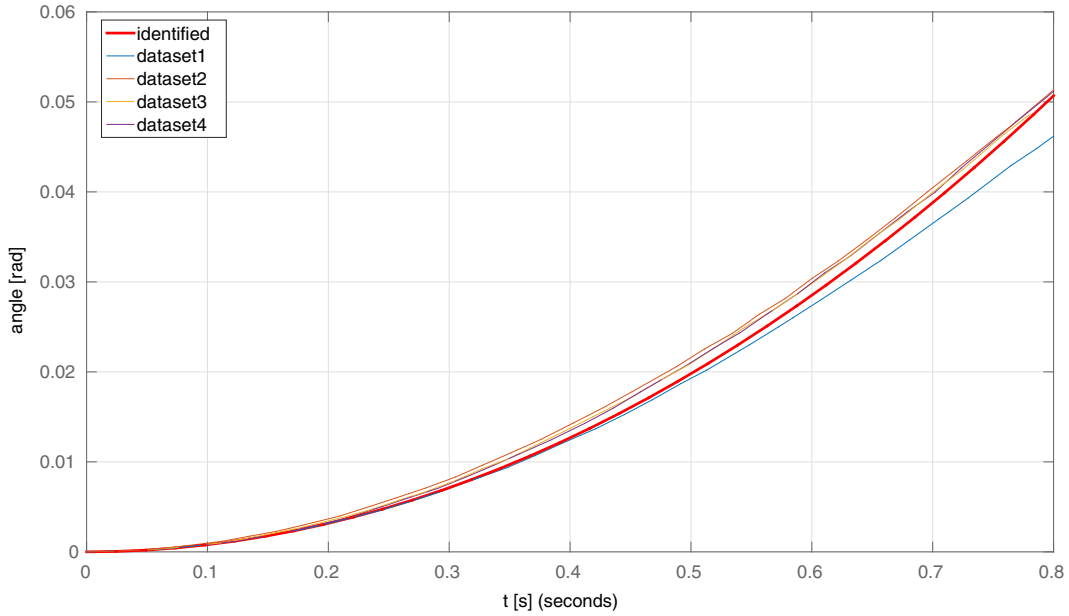

(b) Pitch axis.

Fig. 20 Identification results of the vehicle's moment of inertia. We show roll (**a**) and pitch (**b**) response given the step change in the rolling/pitching moment

velocity measurements due to the vibrations produced by the moving masses. To reduce the noise, we added a first-order low-pass filter ($T_f = 0.02$ s) on the angular velocity measurements.

In Figs. 22 and 23 we give the responses of the roll and pitch angle and the moving masses position, respectively. One can conclude that the rise time of the testbed is almost identical to the rise of the

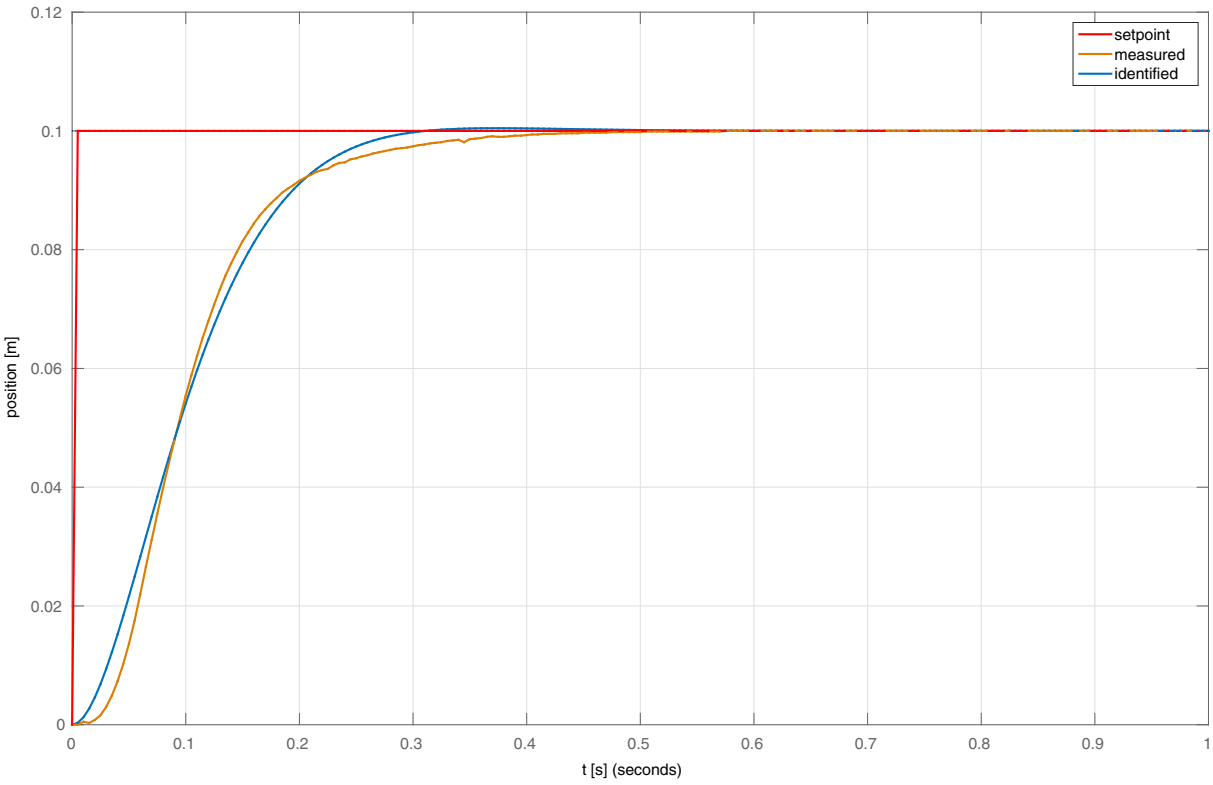

Fig. 21 Identification results of the moving mass dynamics. We give a step setpoint on the moving mass position and identify the transfer function describing the response

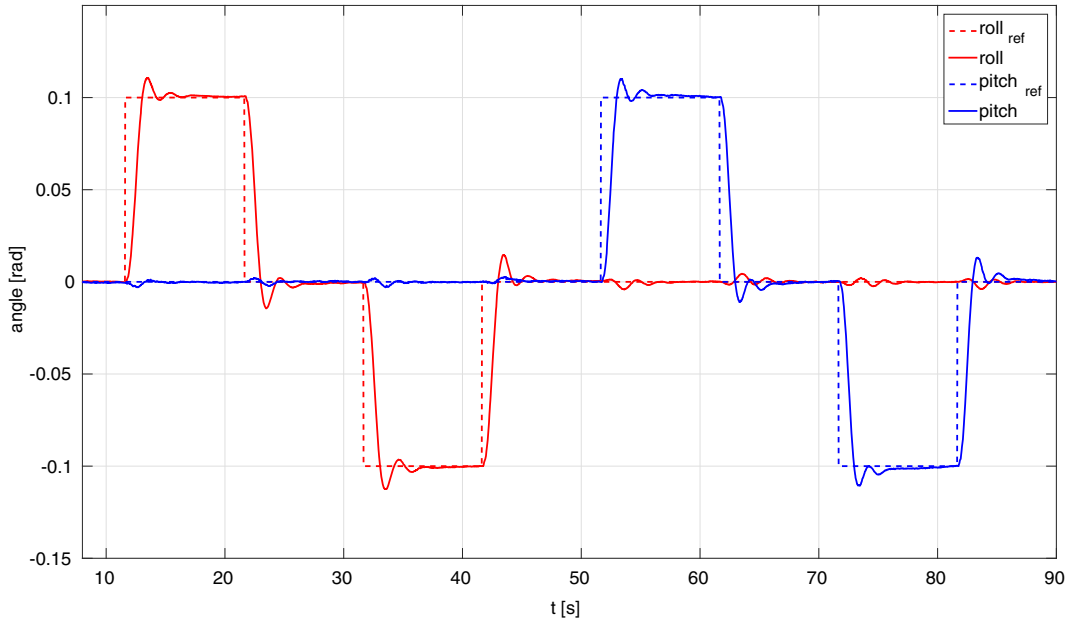

Fig. 22 Roll and pitch step responses of the vehicle mounted on a 2DOF gimbal

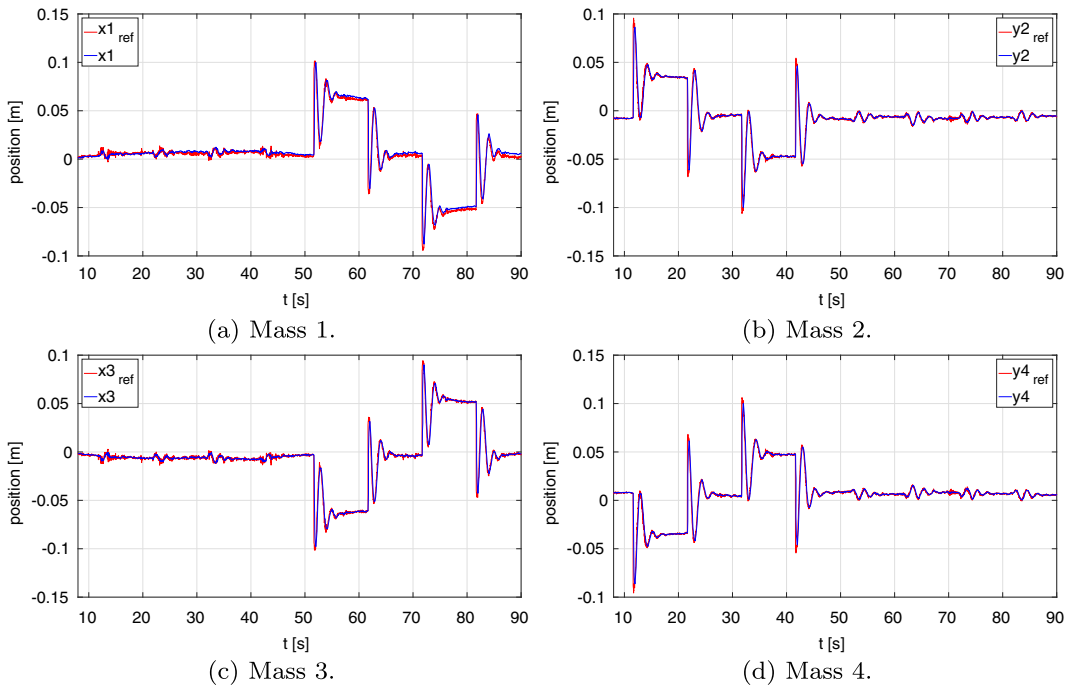

(a) Mass 1. (b) Mass 2. (c) Mass 3. (d) Mass 4.

Fig. 23 Position response of the mass servo system used to control vehicle's roll and pitch angles

simulated vehicle. However, the testbed response is a bit more oscillatory than the simulation response, which is due to added integral component in controllers and low-pass filtering of the feedback signals. The video showing the experiments of the laboratory testbed can be found in [25].

7 Conclusion

In this paper we have presented a novel concept of attitude control for multirotor-UAVs, based on dynamical shifting of vehicle's CoG. The CoG shifting is accomplished through the movement of masses located in the motor arms. We have presented a nonlinear mathematical model and identified dominant components in roll and pitch dynamics. Transfer functions have been derived for the linearized model and stability analysed through root locus. Furthermore, we have given a detailed analysis of multi-rotor UAV dynamical performance as a function of three mechanical parameters. We have defined a metric that reflects the speed of the open loop system, and optimized the metric to get parameters for moving mass weight and maximum displacement. Based on sensitivity and stability analysis, we have determined favourable vertical position of the moving mass plane. Through the analysis in frequency domain we have determined the moving mass servo system dynamics required to stabilize the vehicle. Finally, we have shown the effectiveness of the proposed UAV concept through a simulation in the Gazebo environment and through experiments on a laboratory testbed, consisted of a full-scale vehicle mounted on a 2 DOF gimbal. The presented results demonstrate a good agreement between the theoretical results obtained through linear system analysis and results obtained both in simulation and experimental testbed.

In our future work, we will address the influence of varying rotor dynamics to system stability, which one can expect when the rotor is powered by an internal combustion engine. We will also address the control of roll/pitch dynamics through the combination of rotor speed variations and CoG shift. Finally, we will extend our controller structures with adaptive/robust terms in order to address applications in which system parameters vary, such as object transportation and manipulation.

Acknowledgements This research is sponsored by NATO's Emerging Security Challenges Division in the framework of the Science for Peace and Security Programme as Multi Year Project under G. A. number 984807, named Unmanned system for maritime security and environmental monitoring - MORUS.

References

1. Bouabdallah, S., Murrieri, P., Siegwart, R.: Design and control of an indoor micro quadrotor. In: Proceedings of the 2004 IEEE International Conference on Robotics and Automation, 2004, ICRA04., vol. 5, pp. 4393–4398. IEEE (2004)
2. Menon, S., Moulton, N., Cadou, C.: Development of a dynamometer for measuring small internal-combustion engine performance. J. Propuls. Power **23**(1), 194–202 (2007)
3. Sharaf, O.Z., Orhan, M.F.: An overview of fuel cell technology: Fundamentals and applications. Renew. Sust. Energ. Rev. **32**, 810–853 (2014)
4. Bluteau, B., Briand, R., Patrouix, O.: Design and control of an outdoor autonomous quadrotor powered by a four strokes rc engine. IECON 2006-32nd Annual Conference on IEEE Industrial Electronics, pp. 4136–4240. IEEE (2006)
5. Woolsey, C., Leonard, N.: Moving mass control for underwater vehicles. In: Proceedings of the American Control Conference, 2002, vol. 4, pp. 2824–2829 (2002)
6. Qianchen, Y., Qingzhen, Z., Huiping, Z.: A compound control system of axial moving mass and aerodynamic force for mass moment missile. In: 2011 First International Conference on Instrumentation, Measurement, Computer, Communication and Control, pp. 945–948 (2011)
7. Edwards, T.L., Kaplan, M.H.: Automatic spacecraft detumbling by internal mass motion. AIAA J. **12**(4), 496–502 (1974)
8. Aslanov, V., Bezglasnyi, S.: Gravitational stabilization of a satellite using a movable mass. J. Appl. Math. Mech. **76**(4), 405–412 (2012)
9. Pounds, P.E.I., Bersak, D.R., Dollar, A.M.: Grasping from the air: Hovering capture and load stability. In: Proceedings IEEE Int Robotics and Automation (ICRA) Conf, pp. 2491–2498 (2011)
10. Palunko, I., Fierro, R.: Adaptive control of a quadrotor with dynamic changes in the center of gravity. In: Proceedings 18th IFAC World Congress, vol. 18, pp. 2626–2631 (2011)
11. Kondak, K., Krieger, K., Albu-Schaeffer, A., Schwarzbach, M., Laiacker, M., Rodriguez-Castano, I.M.A., Ollero, A.: Closed-loop behavior of an autonomous helicopter equipped with a robotic arm for aerial manipulation tasks. International Journal of Advanced Robotic Systems (2013)
12. Orsag, M., Korpela, C., Bogdan, S., Oh, P.: Hybrid adaptive control for aerial manipulation. J. Intell. Robot. Syst. **73**(1–4), 693–707 (2014). doi:10.1007/s10846-013-9936-1
13. Goldstein, H., Poole, C., Safko, J.: Classical Mechanics. Addison Wesley (2002)
14. Haus, T., Prkut, N., Borovina, K., Marić, B., Orsag, M., Bogdan, S.: A novel concept of attitude control for large multirotor-uavs based on moving mass control. In: 2016 24th Mediterranean Conference on Control and Automation (MED), pp. 832–839 (2016)
15. Haus, T., Orsag, M., Bogdan, S.: Design considerations for a large quadrotor with moving mass control. In: 2016 International Conference on Unmanned Aircraft Systems (ICUAS), pp. 1327–1334. IEEE (2016)
16. Pounds, P.E., Bersak, D.R., Dollar, A.M.: Stability of small-scale uav helicopters and quadrotors with added payload mass under pid control. Auton. Robot. **33**(1–2), 129–142 (2012)
17. Leishman, R.C., Macdonald, J.C., Beard, R.W., McLain, T.W.: Quadrotors and accelerometers: State estimation with an improved dynamic model. IEEE Control. Syst. **34**(1), 28–41 (2014)
18. Mile HaoXiang Technology Co. Ltd: DLE111 Engine. http://www.chiefaircraft.com/pdf/DLE111MAN.pdf, Accessed: 2017-03-01
19. Aström, K.J., Murray, R.M.: Feedback systems: an introduction for scientists and engineers. Princeton University Press (2010)
20. Meyer, J., Sendobry, A., Kohlbrecher, S., Klingauf, U., von Stryk, O.: Comprehensive simulation of quadrotor uavs using ros and gazebo. In: 3rd Int. Conf. on Simulation, Modeling and Programming for Autonomous Robots (SIMPAR) (2012). to appear
21. Furrer, F., Burri, M., Achtelik, M., Siegwart, R.: Robot operating system (ros), Studies Comp.Intelligence Volume Number:625, vol. The Complete Reference (Volume 1), no. 978-3-319-26052-5, p. Chapter 23. iSBN:978-3-319-26052-5 (2016)
22. Orsag, M., Haus, T., Palunko, I., Bogdan, S.: State estimation, robust control and obstacle avoidance for multicopter in cluttered environments: Euroc experience and results. In: 2015 International Conference on Unmanned Aircraft Systems (ICUAS), pp. 455–461. IEEE (2015)
23. Haus, T., Orsag, M., Bogdan, S.: Visual target localization with the spincopter. J. Intell. Robot. Syst. **74**(1–2), 45–57 (2014). doi:10.1007/s10846-013-9908-5
24. Haus, T., Orsag, M.: Gazebo-based simulator for a multirotor UAV with moving mass control concept. http://github.com/larics/morus_uav_gazebo, Accessed: 2017-02-25
25. Haus, T., Orsag, M.: MORUS UAV with moving mass control - video of simulation and experimental results. goo.gl/dWwsak, Accessed: 2017-03-12

Tomislav Haus received his M.S.E.E. in 2012 and B.S.E.E. in 2010 at the University of Zagreb, Croatia. He is currently employed as Research and Teaching Assistant at the Faculty of Electrical Engineering and Computing, University of Zagreb. He has been working on several international scientific projects, including EU-FP7 projects ASSISIbf and EuRoC, and NATO-SPS project MORUS. His research interests include robotics, unmanned aerial vehicles and multi-agent systems. For his outstanding academic records he won several "Josip Loncar" awards and bronze plaque as well as University of Zagreb Rector Award for the best student projects in 2012. He is a coauthor of several conference and journal papers.

Matko Orsag received his Ph.D. in 2014 and M.S.E.E. in 2008 at the University of Zagreb, Croatia. He is currently employed at the Faculty of Electrical Engineering and Computing, University of Zagreb, as an assistant professor where his teaching duties include both undergraduate and graduate programmes. His main areas of interest are autonomous systems, robotics and intelligent control systems. During his undergraduate years he received several student awards, as well as a bronze plaque "Josip Loncar" for overall outstanding academic achievement. He also received the University of Zagreb Rector Award for the best student projects in 2006. He is a coauthor of multiple conference and journal papers.

Stjepan Bogdan received his Ph.D.E.E. in 1999, M.S.E.E. in 1993 and B.S.E.E. in 1990 at the University of Zagreb, Croatia. Currently he is an associate professor at the Faculty of Electrical Engineering and Computing, University of Zagreb. His main areas of interest are discrete event systems, intelligent control systems, and autonomous systems. He is a coauthor of three books and numerous papers published in journals and proceedings. He serves as associate editor of IEEE Transactions of Automation Science and Engineering, Journal of Intelligent and Robotic Systems, Transactions of the Institute of Measurement and Control and Journal of Control Theory and Applications.